RESEARCH ARTICLE

A 3D molecular map of the cavefish neural plate illuminates eye-field organization and its borders in vertebrates

François Agnès*,‡, Jorge Torres-Paz*, Pauline Michel and Sylvie Rétaux‡

ABSTRACT

The vertebrate retinas originate from a specific anlage in the anterior neural plate called the eye field. Its identity is conferred by a set of 'eye transcription factors', whose combinatorial expression has been overlooked. Here, we use the dimorphic teleost *Astyanax mexicanus*, which develops proper eyes in the wild type and smaller colobomatous eyes in the blind cavefish embryos, to unravel the molecular anatomy of the eye field and its variations within a species. Using a series of markers (*rx3*, *pax6a*, *cxcr4b*, *zic1*, *lhx2*, *emx3* and *nkx2.1a*), we draw a comparative 3D expression map at the end of gastrulation/onset of neurulation, which highlights hyper-regionalization of the eye field into sub-territories of distinct sizes, shapes, cell identities and combinatorial gene expression levels along the three body axes. All these features show significant variations in the cavefish natural mutant. We also discover sub-domains within the prospective telencephalon and characterize cell identities at the frontiers of the eye field. We propose putative fates for some of the characterized eye-field subdivisions, and suggest the existence of a trade-off between some subdivisions in the two *Astyanax* morphs on a micro-evolutionary scale.

KEY WORDS: Eye-field transcription factors, Telencephalon, Hypothalamus, Cell identity, *Astyanax mexicanus*, Natural variation

INTRODUCTION

In vertebrates, the bilateral retinas emerge at the end of gastrulation from a single territory in the neural plate called the eye field and located between the prospective telencephalon and diencephalon (Varga et al., 1999; Woo and Fraser, 1995). At such early stage, the eye field already displays significant variations in size and shape across species, which likely prefigure their future morpho-anatomical differences and probably result from species-specific fine-tuning of earlier inductive and signalling events (Bielen et al., 2017; Rétaux et al., 2013).

During gastrulation, anterior neural fate acquisition and distinction between telencephalon or eye-field identities require antagonizing posterior Wnt signals from the anterior neural border (Heisenberg et al., 2001; Houart et al., 2002, 1998) and restricting Bmp activity in the anterior-most neural ectoderm (Bielen and Houart, 2012). The latter protects the future telencephalon from acquiring eye identity by repressing the expression of the key eye-field transcription factor *rx3* (Bielen and Houart, 2012; Fish et al., 2004; Stigloher et al., 2006; reviewed in Giger and Houart, 2018).

Prior to neurulation, a set of transcription factors, *rx*, *pax6*, *six3*, *six6* and *lhx2*, which are expressed in dynamic and overlapping patterns, define eye-field identity and constitute a self-regulating feedback genetic network, in which *otx2* initially primes the anterior neural plate (ANP) for eye-field formation (Zuber et al., 2003).

During neurulation, ANP cells adopt specific and drastically different migratory behaviours and trajectories according to their identity: dorso-medial convergence for telencephalic progenitors; evagination for eye-field cells; and anterior ward movement for hypothalamic precursors (reviewed by Bazin-Lopez et al., 2015; Sinn and Wittbrodt, 2013; Wilson and Houart, 2004). Eye progenitors undergo complex movements, starting even before the onset of evagination of the bilateral optic vesicles (England et al., 2006). Subdomains of the optic vesicles do maintain their relative positions during morphogenesis (Kwan et al., 2012), suggesting that related, adjacent retina territories might already be determined at late gastrula before evagination.

Anteriorly, the eye field juxtaposes the prospective telencephalon, as revealed by specific markers in zebrafish (Stigloher et al., 2006). By contrast, eye-field posterior limits are less clear, as suggested by *pax6* extending posteriorly to *rx3* (Loosli et al., 2001; Zuber et al., 2003) and overlapping with diencephalic markers (Macdonald et al., 1997; Staudt and Houart, 2007). Thus, *pax6* and *rx3* do not appear to form a uniform optic domain and the other eye-field transcription factors likely add additional combinatorial patterning complexity to the eye field that has yet to be investigated.

Here, we sought to define a 'molecular portrait' of the eye field and determine its exact frontiers with surrounding territories in 3D. For this purpose, we used the embryos of the dimorphic fish *Astyanax mexicanus*, which comes in wild-type (surface fish) and blind troglodytic (cavefish) forms; the comparison of these forms offers an exquisite model system to unravel subtle brain anatomical variations (Rétaux et al., 2016). Our results shed new light on what the eye field is, in terms of size, shape, molecular identity and spatial limits. We discovered an unanticipated degree of eye-field regionalization and atypical zones at the frontiers between major forebrain divisions, and significant variations in the natural cavefish mutant.

RESULTS

Viewing eye-field shape and size in 3D with *rx3*

To date, most reports of eye-field size and shape have used 2D imaging (Fig. 1A-D). In *Astyanax*, the eye field-specific marker *rx3* (Stigloher et al., 2006) delineated a smaller bean-shaped domain, convex anteriorly and concave posteriorly, in cavefish compared with the wild-type surface fish embryos (Fig. 1A-D,K,L). 3D rendering revealed a similar shape ventrally with a midline indentation partially separating the eye field in two lobes; this was less pronounced in cavefish (Movie 1) and undetectable by 2D analyses (Fig. 1E-H). The *rx3* domain showed a 25% reduction of volume in cavefish (Fig. 1M), likely corresponding to a lack of posterior *rx3* expression or a more isotropic size reduction (Fig. 1J-J‴).
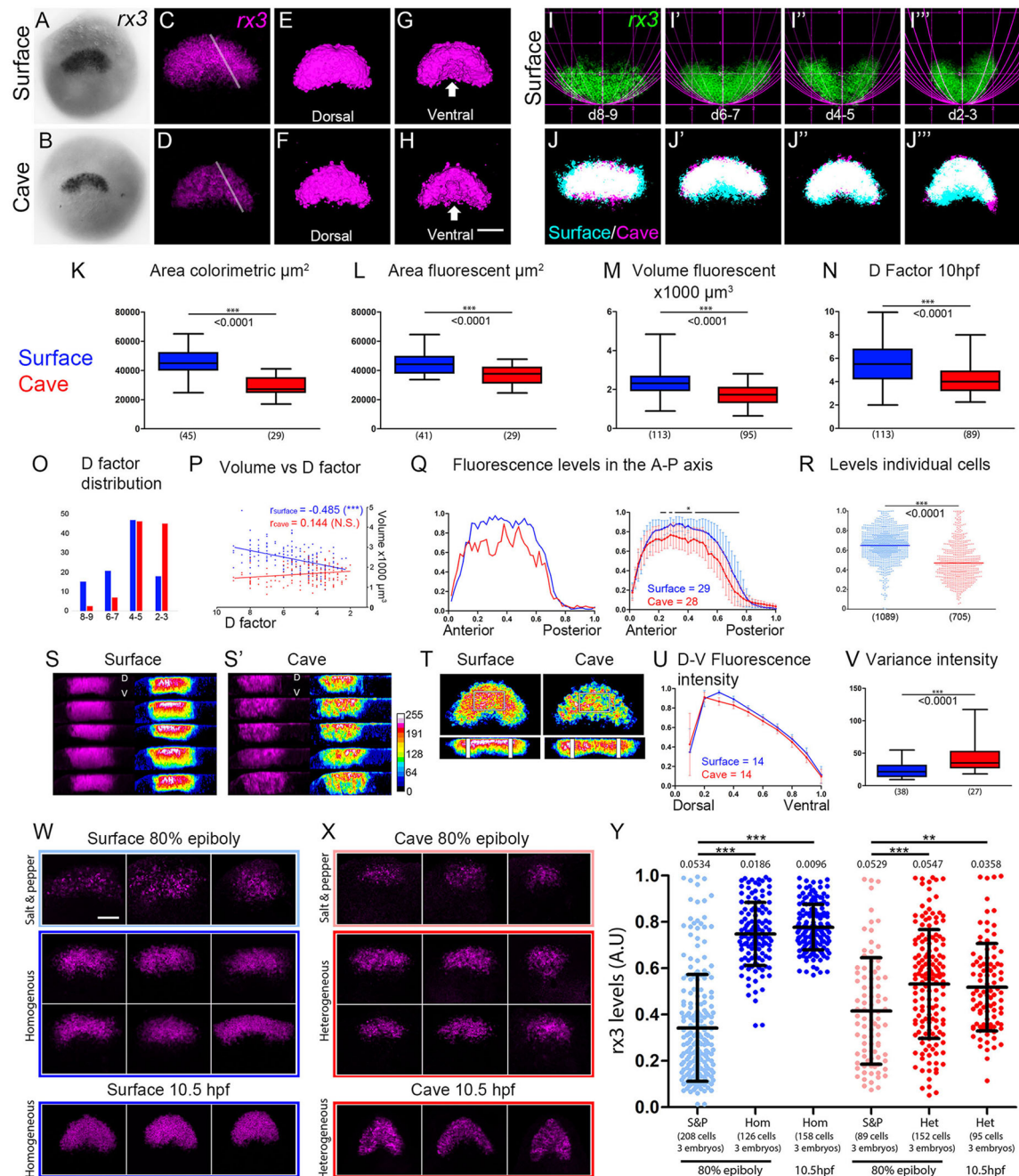
Fig. 1. Characterization of the *rx3* expression pattern in the eye field and neural staging method. (A-J‴) *rx3* expression after colorimetric (A,B) and fluorescent (C-J‴) *in situ* hybridization. (C-J‴) Maximum intensity projections of entire stacks. (C,D) Typical homogeneous and hetereogeous expression patterns of *rx3* and reduction of size in cavefish. (E-H) 3D viewer volume renditions. Arrows indicate ventral medial depletion. (I-I‴) Merges of *rx3* samples (anterior downwards) and their corresponding parabolas of different vertical scaling factors (a=1/d, d=1-8). (J-J‴) Merges of *rx3* expression domain on specimens with a similar d factor. (K,L) Surface areas for *rx3*. (M) Volume of the *rx3*-expressing domain. (N) Mean d factor for embryos fixed at theoretical 10 hpf. (O) d factor distribution at 10 hpf (for same sample size as in M,N). (P) Volume of *rx3* according to d factor. (Q) Plot profiles for *rx3* (lines in C,D) in two representative samples (left) and averaged from many (right). (R) *rx3* levels in individual cells. (S-T) Maximum intensity projections. (S,S′) 3 µm, line in C,D. (T) Dorsal half stack (top) and transverse (bottom) projections. (U) *rx3* levels in the D/V axis (vertical lines, T). (V) *rx3* intensity variance (rectangles in T). (W,X) Maximum intensity projections of entire stacks showing *rx3* pattern for different representative samples at 80% epiboly and 10.5 hpf. (Y) Quantification of *rx3* levels at the single cell level in embryos shown in W,X. All embryos are at 10 hpf, with anterior upwards except I-I‴ and W,X. All pictures (except A,B) are from flat-mounted dissected ANP. Box plots show three quartile dispersion, and minimum and maximum values of the respective datasets. Line histograms in Q (right) and U show averaged mean±s.d. of intensity values for each interval of 0.02 and 0.1 in the *x* axis, respectively. Scale bars: 100 µm.

Eye-field shape and size changes are highly dynamic

We noticed a significant dispersion of eye-field shapes and volumes between samples, all fixed upon their developmental stage and global tailbud morphology at 'theoretical' 10 hpf (Fig. 1I-I‴,J-J‴).

To follow eye-field size and form according to time, we decided to stage ANP *a posteriori* by estimating the advancement of neurulation for each sample. As the anterior ANP curvature resembles a parabola, we designed a simple method to assign

2

each 10 hpf sample with a coefficient (d) that was the inverse of the vertical scaling factor for a parabola. This allowed the classification of samples into subgroups according to their intrinsic morphogenesis progress (Fig. 1I-I‴). Using this method, we found a significant shift towards higher curvatures (lower d factor) for cavefish ANP (Fig. 1N,O). This suggested a heterochrony between the two morphs, with neurulation progression or onset being slightly more advanced in cavefish. To compensate for this bias in sample distribution at 10 hpf, we included older 10.5 hpf surface fish samples in the dataset. This allowed the comparison of eye-field size within the same ranges of d factor for the two morphs (d=2-3 to d=8-9). Whatever the range of d factor, the eye-field volume was always smaller in cavefish, confirming the trend observed at 10 hpf with pooled embryos (Fig. 1P). Furthermore, when comparing size according to d factor, we found a progressive 30% reduction of $rx3^+$ eye-field volume for surface fish (Fig. 1P), whereas the $rx3^+$ volume was constant within the same time interval for cavefish (R^2=0.02). This suggests that the cavefish $rx3$ domain is smaller and does not condense in the same way as it does in surface fish at the onset of neurulation.

Expression of *rx3* within the eye field

Previous analyses showed reduction of *rx3* transcript levels at 10 hpf in cavefish (McGaugh et al., 2014), which we confirmed by RNAseq and fluorescent *in situ* hybridization (not shown; Fig. 1Q). To further investigate intrinsic *rx3* expression pattern and achieve comparisons of spatial distributions of pixel intensities, we used image stack acquisitions to reveal optimized pixels intensities and normalized intensities (see Materials and Methods). Strikingly, *rx3* signals distributed heterogeneously in cavefish embryos when compared with the homogeneous distribution in surface fish (Fig. 1Q-V). Cell-level quantification (Fig. S1, see Materials and Methods) of relative *rx3* signals at 80% epiboly and 10.5 hpf ruled out the hypothesis that cavefish *rx3* expression was blocked in its early expression stage, by distinguishing patchiness at the onset of expression (identical in the two morphs; pale colours, Fig. 1W-Y) from true expression heterogeneity seen only in cavefish. Accordingly, *rx3* fluorescent signals at tail bud stage showed higher dispersions of pixel intensities (Fig. 1V,W) and variance (Fig. 1V,X) in cavefish, with distinct patches of cells, even adjacent, expressing highly variable levels of *rx3* (low to high). This fully penetrant, expression heterogeneity phenotype (*n*=150) was prominent throughout the whole structure (Fig. 1C,D,S′,T,X).

At the tissue scale, *rx3* signals also defined concentric patterns in the A/P and D/V axes (Fig. 1S-T). This pattern was observed at every confocal plane, ruling out maximum intensity projection artefacts (data not shown), and was detected in cavefish, to a lesser extent. In summary, the *rx3* expression domain appears more patterned and complex than previously thought, and shows variation in size, shape, expression intensity and homogeneity between the two *Astyanax* morphs.

cxcr4b identifies a 'core' anterior subdomain within the *rx3*-positive eye field

In zebrafish, *cxcr4a* functions in the segregation of optic vesicles and telencephalon, and its expression depends on *rx3* (Bielen and Houart, 2012). As *rx3* expression was strongly affected in cavefish, we reasoned that this chemokine receptor-encoding gene might be abnormally expressed in cavefish, potentially explaining optic morphogenetic defects. We retrieved *cxcr4a* and *cxcr4b Astyanax* cDNA orthologues (Fig. S2) from our EST library and analysed

cxcr4b (*cxcr4a* was not detected at tailbud stage). In *Astyanax*, the *cxcr4b* bean-shaped expression domain was included within the *rx3*+ eye field in both morphotypes (Fig. 2A-D, Movies 2 and 3) and was 25% smaller in cavefish (Fig. 2H). The *cxcr4b* domain mapped to the anterior dorsal $rx3^+$ region (Fig. 2A-F), identifying a core domain of co-expression, the volume of which was about half that of *rx3* in both morphs. This core region was surrounded in 3D by cells expressing only *rx3* (Fig. 2A-F; Movies 2 and 3), thus highlighting further concentric eye-field patterning (Fig. 1S-T).

Low level *rx3*-expressing cells generally express higher levels of *cxcr4b* in cavefish

As *rx3* expression lacked homogeneity in cavefish (Fig. 1), it became evident that *cxcr4b* and *rx3* expression patterns/levels were complementary within the co-expression domain in cavefish (Fig. 2B-B″,F-F″, Movie 3). Line histogram quantifications confirmed that *rx3*-low zones were *cxcr4b*-high, and vice versa (Fig. 2G-G′). We next quantified pixel intensities in individual cells and plotted relative levels of *rx3* and *cxcr4b* (Fig. 2I-L and Fig. S3). *cxcr4* levels in *cxcr4*-expressing cells were similarly distributed in surface fish and cavefish (Fig. S3B). Nevertheless, the distributions in surface and cavefish were different when plotting *cxcr4b* levels according to *rx3* levels, because of the globally lower *rx3* expression levels in cavefish (Fig. 2J,K and Fig. S3CD). However, in surface fish, the two genes varied together, i.e. *rx3* expression was higher in *cxcr4b*-high cells and *cxcr4b* expression was higher in *rx3*-high cells (Fig. 2L and Fig. S3A). This was not the case in cavefish, where the levels of the two genes varied in an opposite manner, i.e. *rx3* expression was lower in *cxcr4*-high cells and *cxcr4* expression was lower in *rx3*-high cells. These results highlight potential opposing regulatory interactions between *rx3* and *cxcr4b* at the cell population scale in the two morphs.

Shape and size of the *pax6a* domain

We next used the eye-gene marker *pax6*, which, together with *rx3* and *six3*, forms the eye field-specific transcription factor network (Sinn and Wittbrodt, 2013). Specifically, we used *pax6a* (Fig. S4), which is expressed in the eye field (Staudt and Houart, 2007) and in the future posterior retina and diencephalon in zebrafish at 8 somites (Macdonald et al., 1994). At the tailbud stage, in agreement with Strickler et al. (2001), *pax6a* delineated ventral bilateral triangular-shaped domains that were anteriorly and dorsally connected at the midline and showed no expression at the posterior midline, and hence were markedly different from *rx3* (Fig. 3A-B′). In addition, dorsal and ventral projections highlighted *pax6a* domain shape in 3D (Movie 4). The volume of the *pax6a* domain was similar in the two morphs (Fig. 3I). *pax6a* partially overlapped with *rx3* anteriorly and was distributed posteriorly to *rx3* (Fig. 3C,D). The size of the $pax6a^+/rx3^+$ overlapping region was the same in the two morphotypes (Fig. 3L); however, the $pax6a^+/rx3^-$ posterior region was slightly bigger in cavefish (Fig. 3L), suggesting potential trade-off between the anterior and posterior domains. The medio-lateral 'shrinkage' of the *pax6a* from high to low d factors occurred at the same pace in both morphs, ruling out the possibility that neurulation itself was slower in cavefish, and confirming our interpretation that condensation over time is compromised in CF (Fig. S5).

In the medial ANP, the region devoid of both *pax6a* and *rx3* expression (Fig. 3E) was 25% longer in cavefish (Fig. 3J; d=3.5-4.5) but its width was similar on the same samples (Fig. 3J). The resultant 1.6-fold increased aspect ratio (height/width) in
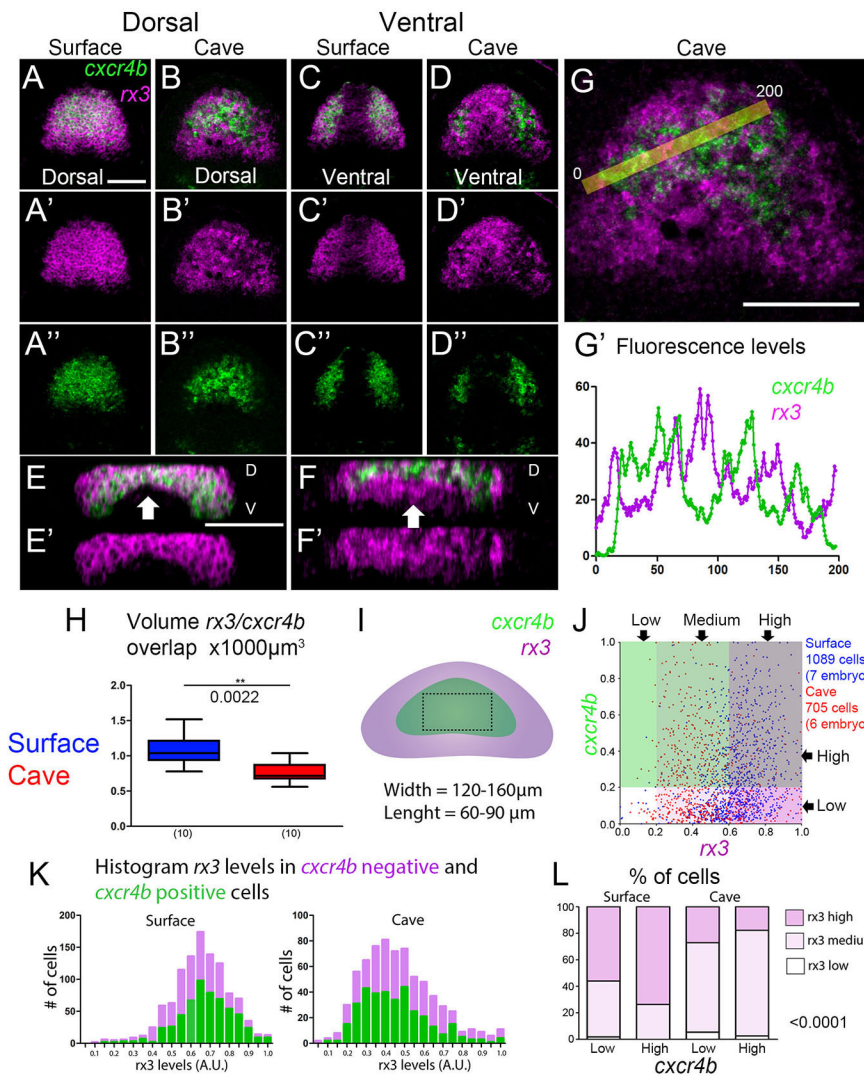
Fig. 2. Characterization of *cxcr4b* expression in relation to *rx3* in the cavefish mutant. (A-G) Maximum intensity projections. (E-F′) Transverse projections. The arrows indicate a larger ventral midline domain expressing only *rx3* in cavefish. (G) Same sample as B, slightly more ventral projection. (G′) Plot profile according to the bar in G. (H) Volume of the *rx3*/*cxcr4b* co-expressing domain. Box plot shows three quartile dispersion, and minimum and maximum values of the datasets. (I) Diagram depicting zones used for 'single cell' quantifications in J-L. (J) Distribution of cells according to intensity levels. (K) Histograms showing frequency of cells positive (green) and negative (magenta) for *cxcr4b* according to *rx3* levels. (L) Distribution of cells expressing different levels of *rx3* according to *cxcr4b*. Scale bars: 100 µm.

cavefish (Fig. 3K), together with the difference in ventral midline shape (Fig. 3), strongly suggested that this ventral medial ANP domain was larger in cavefish. Altogether, these results strengthen the hypothesis that the medial posterior region of the cavefish *rx3* domain is smaller.

pax6a shows anteroposterior and dorso-ventral graded expression patterns

pax6a transcripts distributed in a gradual manner along the anteroposterior axis, with posterior cells showing higher levels than anterior cells (Fig. 3A,B,F). *pax6a* fluorescence intensity in posterior $rx3^+$ cells (A-P position 0.7-0.9 in the *x*-axis) was six times higher than in anterior $rx3^+$ cells (A-P position 0.1-0.3), which was similar in both morphotypes (Fig. 3F). In the intermediate region (0.4-0.6 in the *x*-axis), where the graded expression of *rx3* and *pax6a* shows opposite trends, *pax6a* levels were slightly higher in cavefish, suggesting subtle variations in the control of its expression between the two morphotypes (Fig. 3F, right).

pax6a expression also showed polarization along the D/V axis (Fig. 3G,H). Resliced lateral projections of a region of interest (ROI) (rectangle in Fig. 3E) allowed *pax6a* pixel intensity quantification at four different positions along the A/P axis within the *rx3*-expressing domain [anterior (A), middle (M) and posterior (P)] and outside the *pax6a* domain for background noise (BG) calculation

(Fig. 3G) (see Materials and Methods). Line histograms depicted similar D/V graded expression in the anterior, middle and posterior regions of the $pax6a^+$/$rx3^+$ domain (Fig. 3H). In all three regions, dorsal eye-field cells expressed higher *pax6a* levels than ventral cells. In middle sections, higher *pax6a* levels were observed dorsally in cavefish embryos (Fig. 3H, middle), similar to differences observed in anteroposterior measurements (Fig. 3G, right).

Altogether, these data uncover several additional levels of eye-field regionalization. The graded expression pattern of *pax6a* along the A/P and D/V axes, together with the concentric pattern of *rx3*, suggest unsuspected levels of combinatorial specification within the ANP, which are subtly affected in cavefish.

Defining the posterior limit of the eye field with *barhl2*

As the eye-field markers *rx3* and *pax6a* overlapped only partially, we asked whether the limit of the eye field extended posteriorly to *rx3*. Assuming that *barhl2* is a bona fide marker of the anterior limit of the prospective diencephalon (Staudt and Houart, 2007; Young et al., 2019), we thus used *barhl2* together with *pax6a* and *rx3* to define the posterior eye-field border. As in zebrafish, *barhl2* did not overlap with *rx3* (Fig. S6) and co-labelled several rows (up to eight) of $pax6a^+$ cells at the posterior border of the *pax6a* domain at different stages of neurulation, similarly in both morphotypes
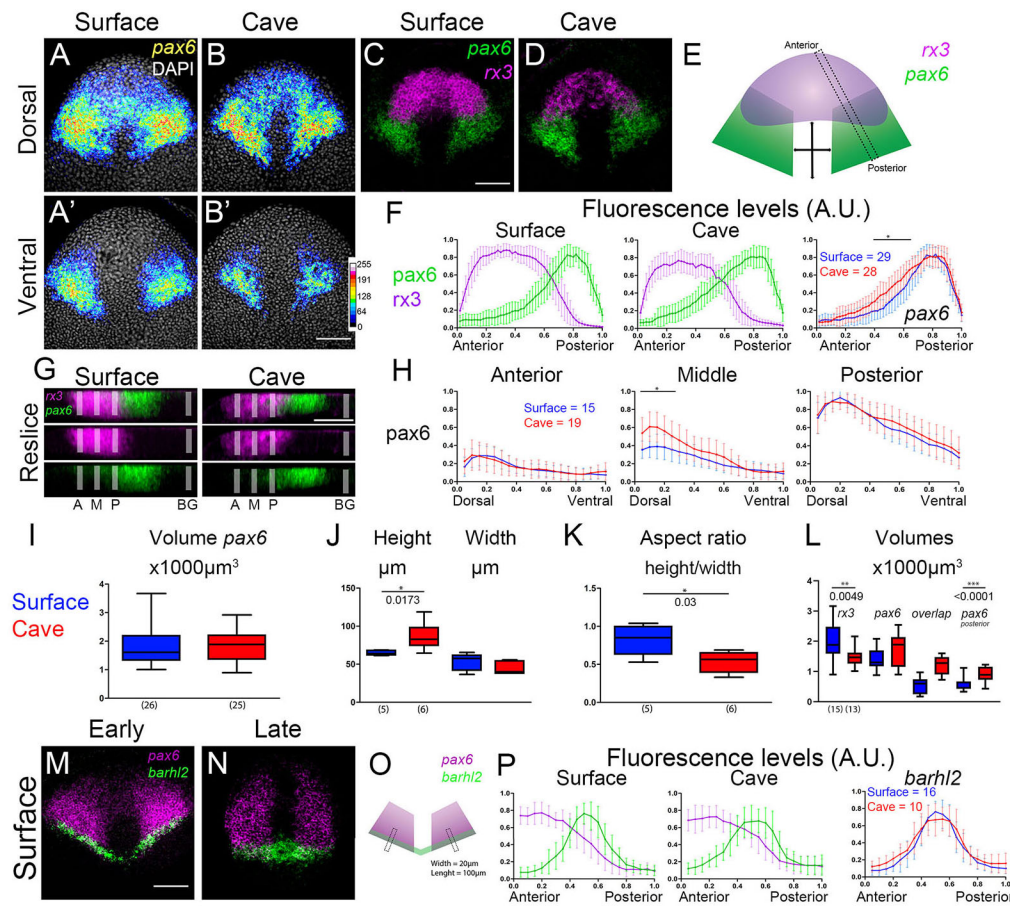
Fig. 3. Characterization of the *pax6a* expression pattern in the eye field and its relationships with *rx3*. (A-D) Maximum intensity projections: (A-B′) 3 µm; (C,D) entire stack. (E) Diagram indicating location of measurements plotted in line histograms (F) and lengths in I and J (double-headed arrows). (F) Plot profile for *rx3* and *pax6a*. (G) Reslice projections (10 µm) for quantification of *pax6a* levels in three positions within the *rx3* domain [A (anterior), M (middle) and P (posterior) positions] and background (BG), according to the line in E. (H) Plot profiles according to A, M and P positions in G. (I) Volume of the *pax6a*-expressing domain. (J,K) Height and width (J), and aspect ratio (K) of the *rx3⁻/pax6a⁻* medial domain (see double-headed arrows in E). (L) Volumes of the *pax6a/rx3* overlapping and *pax6a*-only expressing domains. (M,N) Maximum intensity projections of intermediate substack (3 µm). (O) Diagram indicating location of measurements plotted in the line histograms in P. (P) Plot profiles for *pax6a* and *barhl2* (lines in O). All embryos are at 10 hpf, anterior is upwards. All pictures are from flat-mounted dissected ANP, anterior towards the top. Box plots show three quartile dispersion, and minimum and maximum values of the respective datasets. Line histograms in F, H and P show averaged mean±s.d. of intensity values for each interval in the *x* axis (F=0.02, H, P=0.05). Scale bars: 100 µm.

(Fig. 3M-P). Thus, we deduced that at least two large domains may subdivide the eye field along the anteroposterior axis: an anterior domain containing cells expressing *rx3* with graded levels of *pax6a*; and a posterior domain populated by cells expressing only *pax6a* at high levels. These results suggest that the eye field is not a single territory but a composite tissue.

The ventral limit of the eye field: relative size and position of the hypothalamus

At tailbud stage, the prospective hypothalamus lies just above the prechordal plate and beneath the eye field (England et al., 2006; Pottin et al., 2011; Varga et al., 1999; Wilson and Houart, 2004; Yamamoto et al., 2004). To better characterize the ventral medial frontier of the eye field, we used the hypothalamus marker *nkx2.1a* (Menuet et al., 2007; Yamamoto et al., 2004). The *nkx2.1a⁺* prospective hypothalamus showed expansion in colorimetric *in situ* hybridization (data not shown; Menuet et al., 2007; Yamamoto et al., 2004) and significant increase in volume in cavefish (Fig. 4E).

Assessing the relative spatial arrangement of *rx3* and *nkx2.1a* (Fig. 4A,B) showed no correlation between eye-field curvature (neurulation advancement) and position of the prospective hypothalamus along the A/P axis during the analysed stages (Fig. S7). This suggested that the more anterior position of the *nkx2.1a* domain in cavefish was not due to faster convergence/extension during gastrulation (Torres-Paz et al., 2019), but more likely

to enhanced Shh signalling (Yamamoto et al., 2004). Interestingly, the prospective hypothalamus at 10 hpf had a more-anterior position in cavefish (Fig. 4C,F), showing yet another heterochrony between the two morphs and prompting us to analyse the *rx3/nkx2.1a* frontier zone.

nkx2.1a and *rx3* reveal mixed cell identities at the cavefish hypothalamus/eye-field boundary

Rax and *rx3* expression have been described in the nascent hypothalamus at 14 hpf and E7.5 in zebrafish and mouse, respectively (Loosli et al., 2003; Orquera and de Souza, 2016). In zebrafish tailbud, one study using double *rx3/nkx2.1a* colorimetric staining indicated that some cells might already express the two markers (Tessmar-Raible et al., 2007). The *rx3/nkx2.1a* boundary zone was studied in *Astyanax* samples where at least one-third of the *nkx2.1a* domain had progressed beneath the eye field. In surface fish, *nkx2.1a* and *rx3* had two separate 3D domains that, in most cases, had a medial contact surface (*n*=13/15) with little or no overlap (Movie 5). Conversely, the two domains were always in close contact in cavefish (Fig. 4D-E), suggesting co-expression of *rx3* and *nkx2.1a* in this morph. Indeed, a large *rx3/nkx2.1a* overlapping domain was found in cavefish samples (Fig. 4G, Movie 5), where 'single cell' analysis confirmed the presence of a larger number of cells co-expressing the two markers (Fig. 4H-L) compared with surface fish.

At the tissue level, D/V reconstructions indicated that *rx3⁺/nkx2.1a⁺* cells were mainly located at the *rx3/nkx2.1a*
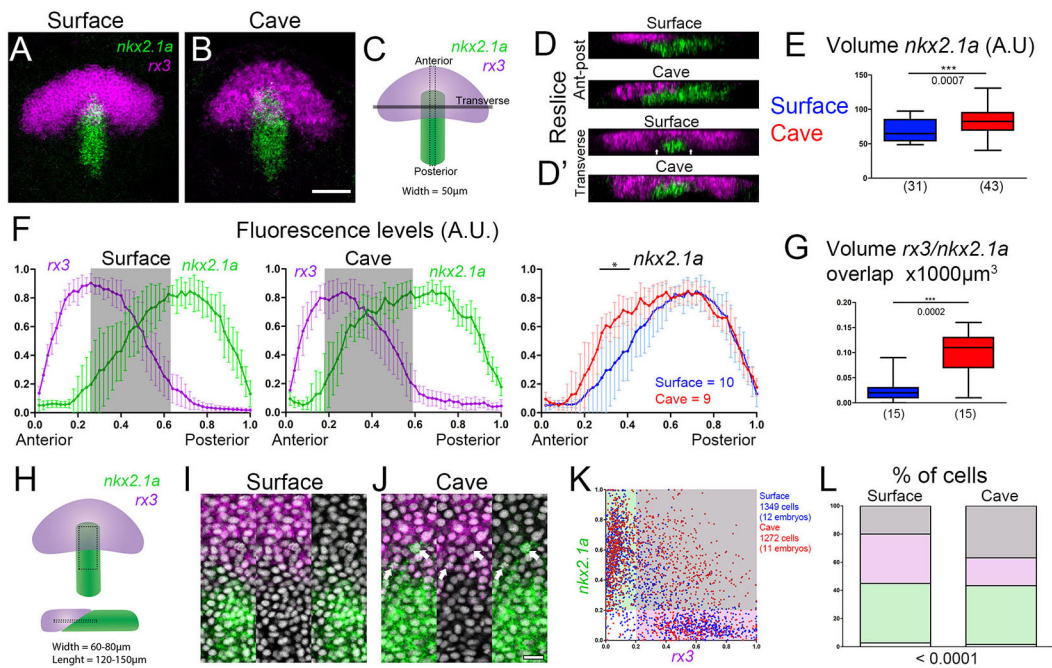
Fig. 4. Characterization of *nkx2.1a* hypothalamic expression pattern and relationships with *rx3*. (A,B) Full stack maximum intensity projections. (C) Diagram for reslices shown in D,D′ and histogram quantification in F (A/P). (D,D′) Reslice projections (1 µm) according to the transverse axis in C. Arrows indicate a gap between *nkx2.1a* and *rx3* domains. (E) Volume of the *nkx2.1a* domain. (F) Plot profile for *nkx2.1a* and *rx3*. Shaded rectangles indicate fluorescence levels above threshold (>0.2). (G) Volume of *nkx2.1a/rx3* co-expressing domain. (H) Diagram for the ROIs used for single cell quantifications in I-L. (I,J) Maximum intensity projections (3 µm). Arrows indicate cells co-expressing *rx3* and *nkx2.1a*. (K) Distribution of cells according to intensity levels. (L) Frequencies of cell populations shown in K. Box plots show three quartile dispersion, and minimum and maximum values of the respective datasets. Line histograms in F show averaged mean±s.d. of intensity values for each 0.02 interval in the *x* axis. Scale bars: 100 µm in B; 20 µm in J.

boundary zone, but some were also found at more dorsal locations within the *rx3*-expressing domain, suggesting aberrant cell specifications (Fig. 4E,I,J). Altogether, these results reveal the existence of a very small subset of *rx3+/nkx2.1a+* cells in the surface fish neural plate at tailbud stage and their increased proportion in cavefish, which could be a direct consequence of increased Shh signalling in cavefish at this stage (Pottin et al., 2011; Torres-Paz et al., 2019; Yamamoto et al., 2004).

Finally, on the lateral sides of the nascent basal hypothalamus, a clear gap separated the *nkx2.1a+* cells from the *rx3+* cells anteriorly (Fig. 4D,D′, arrows; *n*=15/15 surface fish) or from the *pax6a+* cells more posteriorly in all embryos (Fig. S8). This suggests an additional unknown molecular identity in this thin tissue layer that could be the prospective alar hypothalamus based on absence of *nkx2.1a* expression.

Shape and size of the *zic1* domain
We reasoned that *zic1*, which is expressed in retinal precursors at tailbud stage (Devos et al., 2021; Grinblat et al., 1998; Varga et al., 1999) and also responds to midline signalling in zebrafish forebrain (Maurus and Harris, 2009), would help further characterize the eye field molecularly. In *Astyanax*, *zic1* expression delineated an anteriorly convex bean-shaped domain at tailbud stage, similar in shape but more indented ventro-medially than the *rx3* domain (Fig. 5A,B; Movie 6). The *zic1* domain was larger than *rx3* in both morphotypes (Fig. 5A-B″; compare Figs 1M and 5F) regardless of the d factor range considered (not shown). The *zic1* domain showed a 25% reduction in volume in cavefish (Fig. 5F), which likely corresponded to the lack of a posterior medial region (Fig. 5A,B, arrows, Movie 6). We also found a 35% progressive reduction of *zic1+* domain volume for surface

fish as neurulation progressed, whereas it was constant within the same interval for cavefish (surface fish $R2$=0.4039, P<0.001; cavefish $R2$=0.0456, non significant). As for *rx3*, the cavefish *zic1*-expressing domain did not reduce in size in relation to the d factor as it did in surface fish embryos at the onset of neurulation.

zic1 identifies two major domains in the eye field
The *zic1* marker, together with *rx3*, identified three subdivisions within the ANP (Fig. 5A,B). Anteriorly, *zic1* extended beyond *rx3* in both morphs (Fig. 5D,E, blue, Movies 6 and 7), in a zone corresponding to *emx3+* telencephalic precursors (see Fig. 7). The size of this *zic1+/rx3−* telencephalic region was 30% smaller in cavefish regardless of the d factor considered (Fig. 5H). A second zone, composed of *zic1+/rx3+* cells, corresponded to a sub-territory of the *rx3* domain, and was also smaller in cavefish (Fig. 5D,E, red; Fig. 5H, Movie 7). The third medial region (Fig. 5A-C) was populated with *rx3+/zic1−* cells (Fig. 5D,E, white and arrowheads, Movie 7) and was twice as large both in surface area and volume in cavefish embryos (Fig. 5G,J). Proportionally, this domain was fourfold larger in size relative to either *zic1+/rx3−* or *zic1+/rx3+* domains in cavefish.

Thus, two major subdivisions arise in the eye field based on the combination of *zic1* and *rx3* expression (Fig. 5D,E, red/white) and the relative proportions of these two subdivisions vary between the two morphs, suggesting a potential trade-off mechanism within the optic primordium.

Refining eye field lateral posterior subdivisions with *zic1*
Closer inspection of the posterior lateral eye field revealed that *zic1* expression extended slightly posteriorly to *rx3* in the lateral region of surface fish embryos (Fig. 5, arrows; Fig. S9).
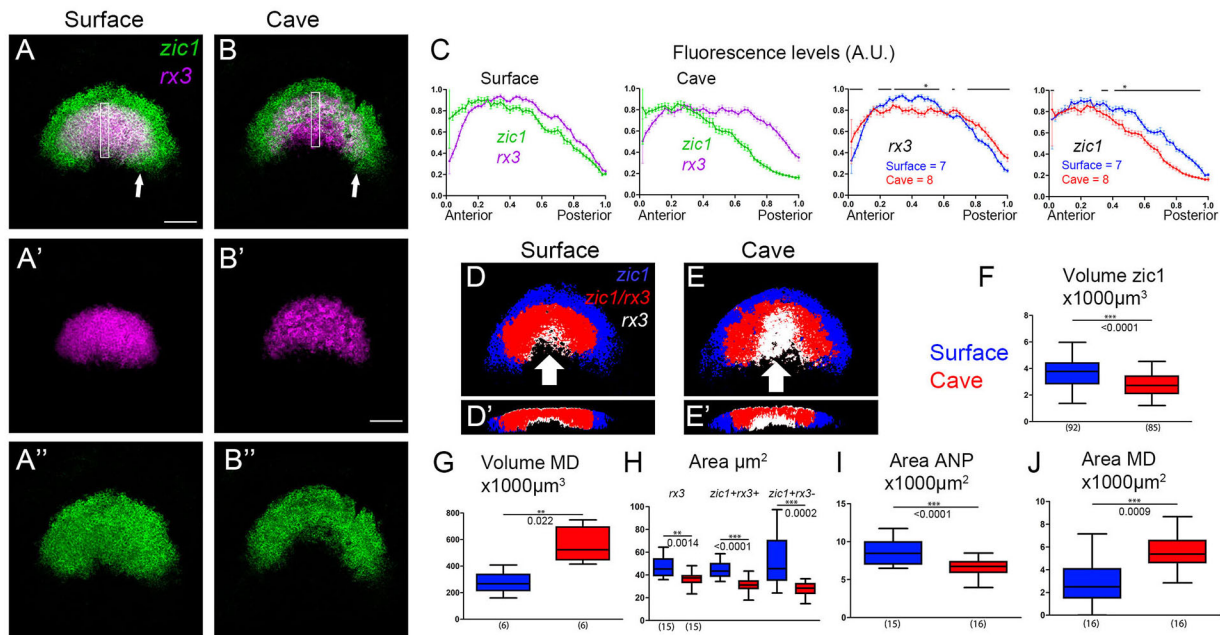
Fig. 5. Characterization of *zic1* expression and identification of eye-field subdivisions. (A-B″) Full stack maximum intensity projections. (C) Plot profiles for *zic1* and *rx3* (rectangles in A,B). (D-E′) Binarized images of 3 μm mid-stack projections showing *zic1* (blue), *zic1* and *rx3* (red), and *rx3*-only (white) segmented domains and transverse sections (D′,E′). (F) Volume of the *zic1*-expressing domain. (G) Volume of the *rx3*-only expressing domain (MD). (H) Relative proportion of surface areas shown in D and E for indicated domains. (I) Total surface area for *zic1*-expressing and *rx3*-expressing domains shown in D and E as a proxy of ANP size. (J) Surface area for the *rx3*-only expressing domain (D,E). Box plots show three quartile dispersion, and minimum and maximum values of the respective datasets. Line histograms in C show averaged mean±s.d. of intensity values for each 0.02 interval in the *x*-axis. Scale bars: 100 μm.

3D analysis confirmed this pattern along the entire DV axis. This additional molecular identity (e.g. *zic1*⁺/*rx3*⁻/*pax6a*⁺ cells) suggested further compartmentalization of the eye field lateral posterior regions (Movies 6 and 7). Reduction of this domain in cavefish, shown by line histogram quantifications (Fig. S9), points to another probable regionalized cell specification variation in the ANP.

zic1, *emx3* and *lhx2* subdivide the telencephalon in three domains

As *zic1* expression extended more anteriorly than *rx3*, we wished to better characterize the anterior eye-field boundary and the presumptive telencephalon, suspecting the telencephalon to be subdivided in different molecular territories as well. We used combinations of markers, including *zic1*, *lhx2* (differentially expressed in the cavefish ANP; Pottin et al., 2011), *rx3* (eye field specific) and *emx3* (telencephalon specific; Houart et al., 1998; Morita et al., 1995). *Lhx2* had a similar pattern to *rx3*, but the *lhx2*/*rx3* pair revealed that the *lhx2* anterior limit systematically exceeded that of *rx3* to the same extent in surface fish and cavefish (Fig. 6A,G, Fig. S10, Movie 8). The *lhx2* domain was 20% smaller in cavefish (Fig. 6E), but the relative volume proportions of the *rx3* and *lhx2* domains remained similar to surface fish (Fig. 6F,H). Using *emx3*, the domain size of which was not significantly different between the two morphs (Fig. 6I), we observed a reduction in telencephalic size according to increased curvature in surface fish, as opposed to a constant volume in cavefish at decreasing d factors (Fig. 6J). This trend was similar to our observations for the *rx3*⁺ eye field (Fig. 1P). We then confirmed that the anterior most *lhx2*-expressing cells (*rx3*⁻) circumferentially mapped to the posterior part of *emx3* domain, in the two morphs (Fig. 6B,G, second plot). The *zic1* anterior limit also laid posteriorly to the *emx3* anterior border

similarly in the two morphs (Fig. 6C,G, third plot and data not shown). Moreover, we established that the *zic1* domain extended beyond the anterior limit of *lhx2*, which was similar in the two morphs (Fig. 6D,G, fourth plot). We also confirmed the existence of an anterior ANP territory composed of *emx3*⁺/*dlx3b*⁺ cells at the telencephalic/placodal boundary (Toro and Varga, 2007; Fig. S11). Finally, we noticed a small subset of cells co-expressing *emx3* and *pax6a* in the small latero-posterior 'arms' of the horseshoe-shaped *emx3* domain (Fig. S12), which may correspond to dorsal posterior telencephalon or epithalamus according to the fate map of Staudt et al. (2019). Altogether, these mappings strongly suggest that the prospective telencephalon at neural plate stage is patterned in several subdomains that potentially correspond to different fates (see Fig. 8).

A 'low-*zic1* crescent' in the anterior ANP is affected in cavefish

We then focused on the eye field/telencephalic boundary. *zic1* showed a thin zone of lowered expression at the putative telencephalic/eye-field border in some samples (Fig. 6L-L‴). This phenotype was rare in surface fish (*n*=3/50, 6%) and more penetrant in cavefish (*n*=15/58, 25%). This was reminiscent of a potential neurulation heterochrony effect in sample distribution (see Fig. 1O). Accordingly, the presence of the 'low-*zic1* crescent' was related to the d factor and its penetrance increased at later neurulation stages in the two morphs (Fig. 6K). Using a qualitative classification of absent, weak, mild or strong (Fig. 6L-L‴), we found a significant increase and full expressivity of the 'low-*zic1* crescent' in cavefish for samples with a low d factor (Fig. 6M). Thus, *zic1* downregulation in this particular domain is temporally similar in the two morphs but spatially different.

To characterize molecularly the thin 'low-*zic1* crescent', we performed 3D renditions, which suggested that it matched the
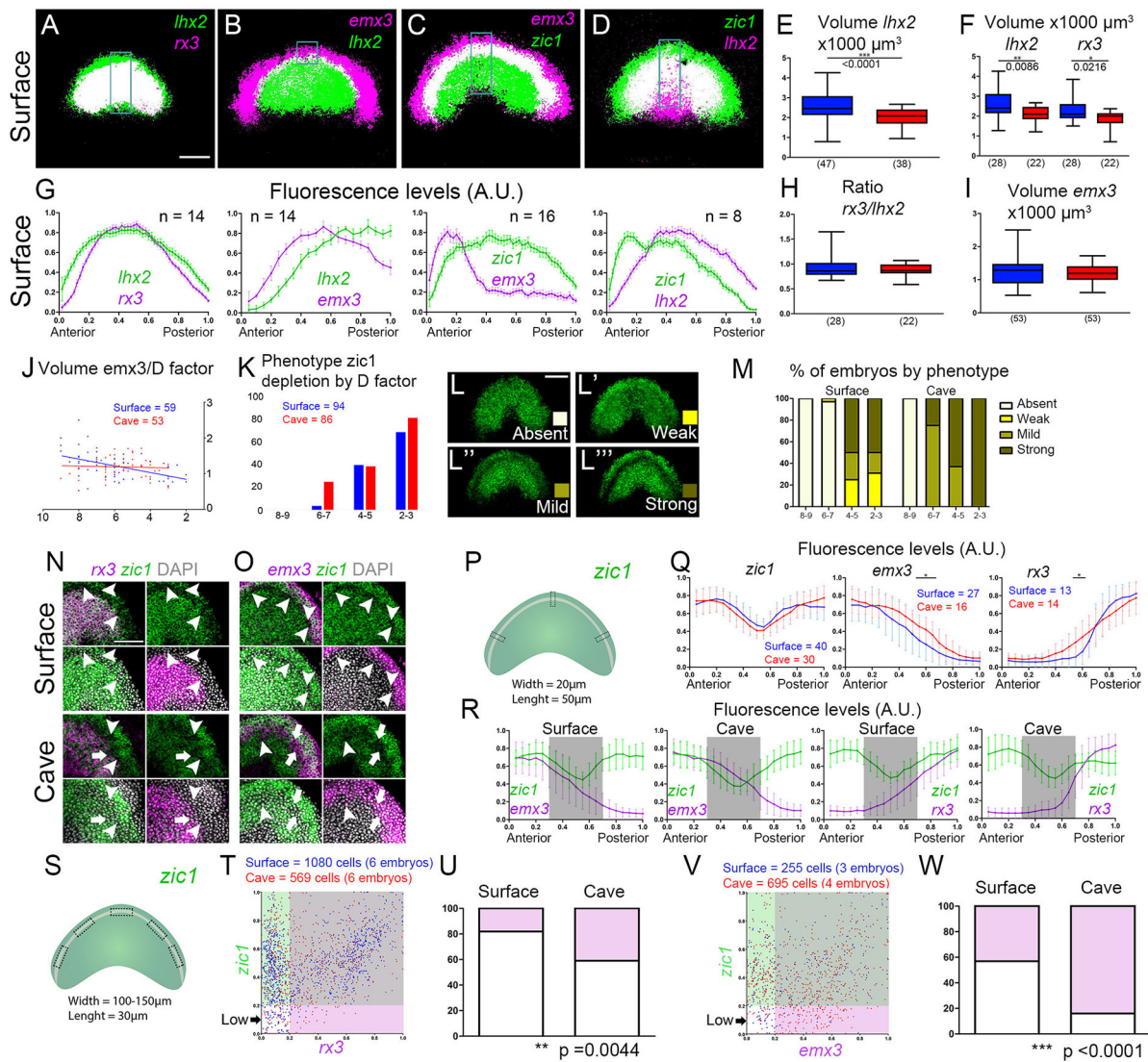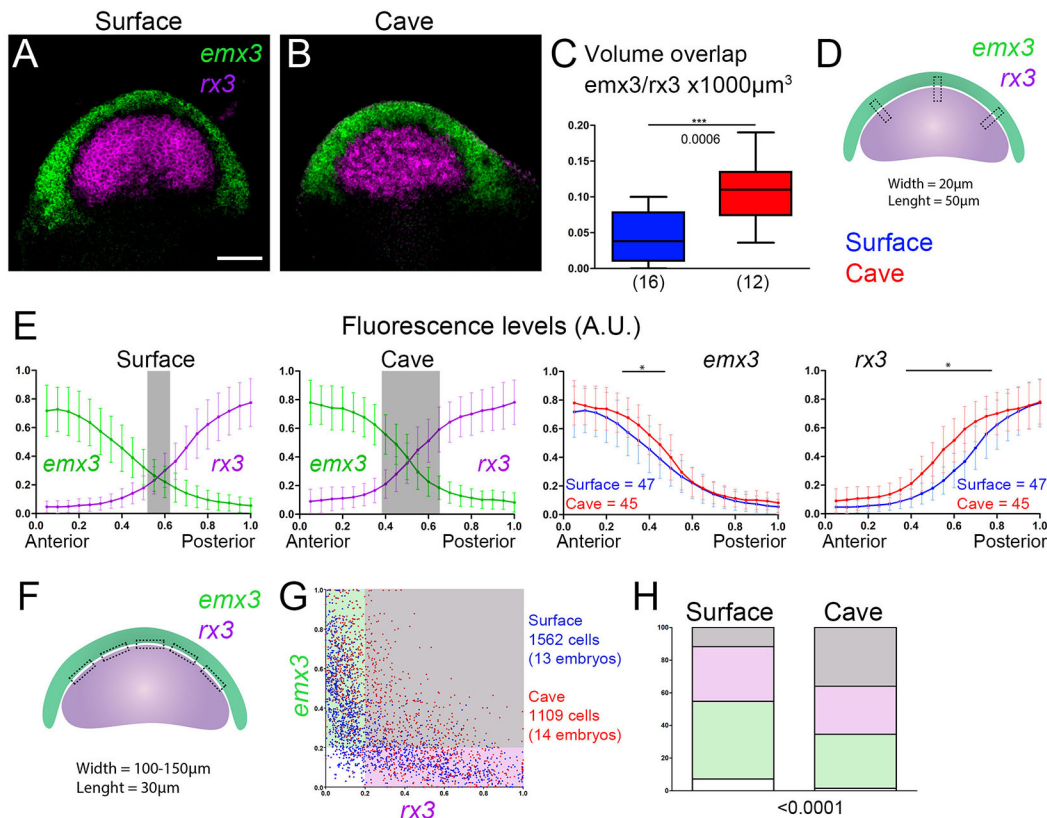
Fig. 6. Identification of telencephalic subdivisions and characterization of the eye field/telencephalon transition zone. (A-D) Binary images of full stack maximum intensity projections. (E-I) Surface and cave plots are, respectively, in blue and red. (E) Volume of the *lhx2* expression domain. (F) Volume of *lhx2* and *rx3* used for the ratio in H. (G) Plot profiles of A-D according to ROIs (rectangles). (H) Ratio of *rx3/lhx2* volumes. (I) Volume of the *emx3* expression domain. (J) Volume of the *emx3* domain according to d factor. (K) Frequency of the *zic1* depletion phenotype according to d factors. (L-L‴) *zic1* depletion categories. (M) Expressivity of each *zic1* depletion category (L-L‴) for the indicated d factors. (N,O) Maximum intensity projections. Arrowheads indicate various *zic1*-depleted zones. Arrows indicate *zic1*-depleted zones with increased *rx3* or *emx3* levels in cavefish. (P) Diagram of the selection of ROIs used to generate the fluorescence plot profiles shown in Q and R. (Q,R) Plot profiles at the *zic1*-depletion zone for *zic1*, *emx3* and *rx3*. (R) Shaded rectangles indicate the *zic1*-depletion zone. (S) Diagram of the ROIs used for single cell quantifications. (T,V) Distribution of cells according to intensity levels. Coloured areas refer to marker thresholds. (U,W) Frequencies of cell populations shown in T and V using the same colour code. Anterior is towards the top. Box plots show three quartile dispersion, plus minimum and maximum values of the respective datasets. Line histograms in G (2nd graph), and Q, R and G (1st, 3rd and 4th graph, respectively) show averaged mean±s.d. of intensity values for each 0.05 and 0.02 interval in the *x* axis, respectively. Scale bars: 100 μm in A-D,L; 50 μm in N.

eye field/prospective telencephalon border, forming a gap between the two territories (Fig. 6N,O; Movie 6). Line histograms drawn across the zone of interest in 2 μm projections of ANPs stained for *zic1/emx3* or *zic1/rx3* (Fig. 6P) showed similar profiles for *zic1* in the two morphs (Fig. 6Q, left), further confirming the shared characteristics of the *zic1*-depleted region for samples of similar morphogenetic stages. Intensity profiles of *emx3* and *rx3* showed that the 'low-*zic1* crescent' potentially had a prospective telencephalic identity in surface fish, as deduced from intermediate *emx3* levels and very low or no *rx3* expression (Fig. 6R, first and third plots, respectively).

Strikingly, both the relative levels of *emx3* and *rx3* were elevated in the 'low-*zic1* crescent' in cavefish (Fig. 6Q,R, second and fourth plots, respectively), suggesting improper cell specification in this eye field/telencephalon intermediate region. These profiles may also be interpreted as the result of posterior and anterior shift of the *emx3* and *rx3* limits, respectively, in cavefish. We thus used 'single cell' analysis to quantify relative pixel intensities in the *zic1*-depleted zone (Fig. 6S). In this domain (indicated as 'Low' in Fig. 6T,V), a fraction of cells expressed significant levels of *rx3* (~20% in surface and 40% in cavefish; Fig. 6T,U). We also identified some *emx3*-expressing cells within this domain, which corresponded to ~40% in surface fish

Fig. 7. Identification of telencephalic subdivisions and characterization of the eye field/telencephalon transition zone. (A,B) Full stack maximum intensity projections. (C) Volume of overlapping domain. (D) Diagram of the ROIs used to generate plot profiles shown in E. (E) Plot profiles for emx3 and rx3. Shaded rectangles indicate levels above threshold (>0.2). The third and fourth plots compare expression at the boundary of emx3 and rx3. (F) Diagram of the ROIs used for single cell quantifications. (G) Distribution of cells according to intensity levels. Coloured areas refer to marker thresholds. (H) Frequencies of cell populations shown in G using same colour code. Box plot shows three quartile dispersion, and minimum and maximum values of the respective dataset. Line histograms in E show averaged mean±s.d. of intensity values for each 0.05 interval in the x axis.

embryos and 80% in cavefish (Fig. 6V,W). Such a high proportion of cells expressing emx3 in the 'low-zic1 crescent' strongly suggested that the emx3 posterior boundary was slightly shifted posteriorly in cavefish. Altogether, these data characterize a previously unreported zone in the ANP, showing subtle differences in cavefish, with temporal and molecular shifts of the 'low-zic1 crescent'.

Mixed cell identities at the eye field/telencephalon boundary in cavefish

Finally, we analysed the telencephalic/eye-field boundary proper. In surface fish, we observed a fully penetrant gap between the rx3 and emx3 domains (Fig. 7A, Movie 9), which was independent of the neurulation stage/d factor (not shown). Line histogram quantifications confirmed low (<0.2) relative pixel intensities at the intersection of the two curves (Fig. 7D,E, first plot). Strikingly, this emx3⁻/rx3⁻ gap zone was never detected in cavefish (Fig. 7B, Movie 9), and line histograms revealed significantly higher relative pixel intensity levels for both markers at the intersection zone (Fig. 7E, second plot).

Comparison of emx3 and rx3 fluorescence intensity curves revealed a slight posterior and anterior shift, respectively, in cavefish (Fig. 7E, right plots). Accordingly, volume analyses detected a significant emx3/rx3 overlapping domain in cavefish (Fig. 7C). Furthermore, 'single cell' analysis at the interface zone (Fig. 7F) showed a threefold increase in the proportion of cells expressing medium to high relative levels of both emx3 and rx3 in

cavefish (Fig. 7G,H, grey), indicating a high degree of co-expression. We also found in cavefish a fivefold decrease in the percentage of cells expressing low levels for both markers (Fig. 7G,H, white), consistent with the absence of gap observed at the telencephalic/eye-field interface in this morph. In sum, this peculiar 'gap zone' expressing the lowest levels of rx3 and emx3 in surface fish might correspond to another yet undescribed ANP subdivision that, again, seems phenotypically affected in cavefish.

DISCUSSION
What is the eye field?

Studies in different models have suggested that the vertebrate eye field is specified by a combination of several transcription factors (Varga et al., 1999; Zuber et al., 2003). Accordingly, pax6, lhx2 or rx3 are considered as interchangeable markers and universal 'master' eye genes, a notion that fits well with the absence of eye development and anophthalmic phenotype of knockout/mutant animals (Gehring, 1996; Loosli et al., 2001; Porter et al., 1997). Our 3D expression map reveals unsuspected and extensive eye-field regionalization at late gastrula stage. Using combinations of five markers, we identified six subdomains in which pax6a graded expression patterns (A/P, D/V) superimposed an additional degree of patterning complexity (Fig. 8).

The rx3/pax6a coupling identified three major eye-field subdivisions in the A/P axis: an anterior rx3-only zone; an intermediate rx3⁺/pax6a⁺ zone and a posterior pax6a-only zone. The last was distinct from the anterior prospective diencephalon
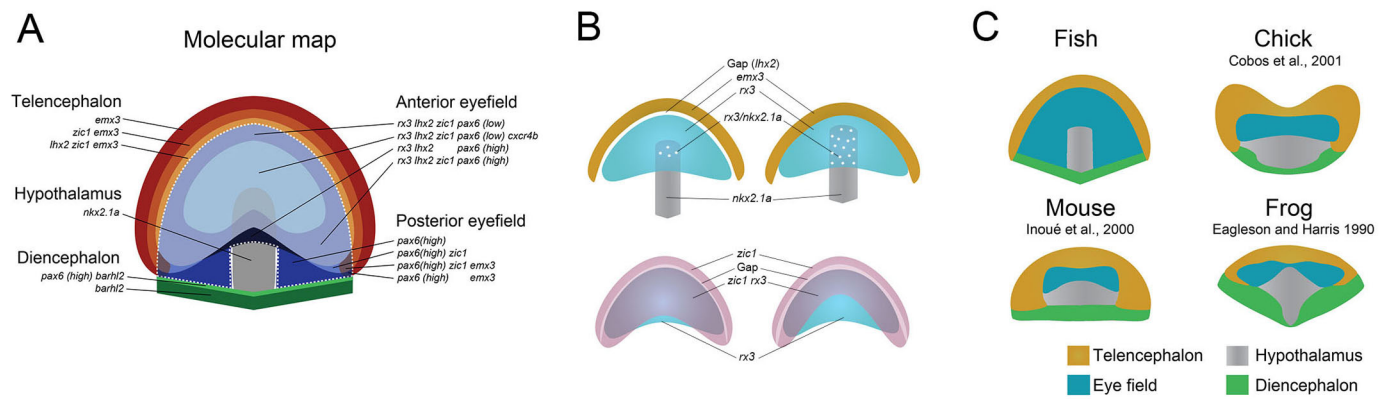
Fig. 8. Molecular map of the ANP and modifications observed in the *Astyanax* morphs. (A) ANP major divisions and further subdivisions of the eye field and prospective telencephalon and respective molecular identities. The dashed line delineates the eye field. (B) Comparison of salient phenotypes in the two *Astyanax* morphotypes. (Top) A clear gap separates eye field and telencephalic territories in surface fish (left), whereas they are joined in cavefish (right). The ventral eye field and hypothalamus domain appose in surface fish (left), whereas they are intermingled in cavefish (right, white dots). The prospective hypothalamus is larger and is located more anteriorly in cavefish. (Bottom) The zone of *zic1* depletion (Gap) at the eye field/telencephalon boundary appears earlier and is wider in cavefish. The midline domain expressing *rx3* only shows expansion in cavefish. (C) ANP anatomical variations across evolution in vertebrates. The main prospective forebrain subdivisions and relative proportions are shown.

barhl2+ border at tail bud stage. The *rx3/zic1* coupling defined three subdivisions in the medio-lateral axis: a medial *rx3*-only zone, an intermediate *rx3*+/*zic1*+ zone and a small lateral posterior *zic1*-only zone. Additional positional information is given by the *pax6a* graded expression patterns (D/V and A/P), the *rx3/zic1* combination in the medial region and the anterior *cxcr4*-expressing core. These molecularly defined eye-field subdomains integrate in a theoretical framework of forebrain development, which results from potential causal signalling effects (Rubenstein et al., 1998). The eye field should thus be modelled as a highly regionalized structure, well before its bilateral evagination into two optic vesicles. It is likely that many more distinct eye-field cell identities, defined by combinatorial expression of additional transcription factors, are already specified at late gastrula.

The optic recess region (ORR) has been proposed as a morphogenetic entity organized around the optic recess, between the hypothalamus and telencephalon, that could be derived from the eye field (Affaticati et al., 2015). Under this framework, we suggest fates for some of the eye-field subdivisions, in view of the comparative and quantitative observations made in our model. Importantly, these hypotheses are based solely on expression patterns and will need further tracking and lineage analyses for confirmation. The *rx3*+/*zic1*+/*pax6a*+ cells would represent the anterior eye fields potentially fated to become retinas, which are smaller in cavefish (Alunni et al., 2007; Devos et al., 2021; Yamamoto and Jeffery, 2000). The posterior *rx3*−/*pax6a*+/*barhl2*−/*emx3*− eye-field cells, subdivided in at least two populations (*zic1*+ and *zic1*−), would be potentially fated to become posterior retinas and RPE. By contrast, the medial *rx3*+/*zic1*− cells, which occupy a larger territory in cavefish, could prefigure the medial ORR/alar hypothalamus and the optic stalk region, both larger in cavefish at 24 hpf (Torres-Paz et al., 2019). The relative sizes of these eye-field derivatives would vary between the two morphs, as a trade-off within the optic primordium, likely because of variations in signalling (Torres-Paz et al., 2019). Given the homology and similar molecular organization of the ANP in vertebrates, our data also let us predict a similar extent of ANP regionalization and variation in different species (Fig. 8C).

Our study also highlights subdomains of the prospective telencephalon, which, like the prospective diencephalon (Staudt

and Houart, 2007) and eye field (this study), is composed of several concentric territories of specific cell identities, suggesting distinct cell fates. Our proposed ANP molecular map, which integrates concentric gene expression, as previously suggested (Toro and Varga, 2007; Zuber et al., 2003) (Fig. 8), will be relevant to spatially interpret future single cell transcriptomics analyses of developmental trajectories.

Variations at the borders
A prospective telencephalon/eye-field boundary
Surprisingly, our 3D confocal analysis reveals a small previously unreported, two or three cells wide circumferential territory separating prospective telencephalon (*emx3*+) and eye field (*rx3*+), and expressing both markers at low levels in surface fish tailbud (Fig. 7, Movie 9). In cavefish, this region showed cells with mixed identity, i.e. higher relative levels for both markers compared with surface fish. As higher *emx3* relative levels might repress *rx3*, which is itself expressed at low levels in cavefish, this suggests that progenitors at the border are likely to adopt a telencephalic fate later on. Similar prospective telencephalon size in both morphotypes invalidates a slight posterior telencephalic expansion hypothesis, but not a potential progressive telencephalic fate adoption in cavefish. Interestingly, this tiny region also corresponds to the 'low-*zic1* crescent', which is larger and has different expression dynamics in cavefish. Together, these findings suggest two non-mutually exclusive models: (1) progenitors at the border region maintain dual cell fate potentiality at tailbud stage that is resolved later on; or (2) this region would constitute an uncovered anterior subdivision of the neural plate with specific (unknown) cell fate. Fgf and Hedgehog signalling (Cavodeassi and Houart, 2012), which are both subtly modified in cavefish (Pottin et al., 2011; Yamamoto et al., 2004), are good candidates for explaining variations observed at the telencephalon/eye field boundary between the two morphs.

Mixed identities at the hypothalamus/eye-field boundary
In surface fish, only a few cells at the eye field/hypothalamus contact zone express *rx3* and *nkx2.1a* at tailbud stage. Therefore, they may prefigure anterior/tuberal hypothalamic neuropeptidergic fates (Muthu et al., 2016). In cavefish, this intersection is doubled in size, which agrees with reported variations in neuropeptidergic

10

neuroanatomy in the basal forebrain of the two *Astyanax* morphs. *shh*, the expression of which is expanded in cavefish prechordal plate at this stage (Pottin et al., 2011; Ren et al., 2018; Torres-Paz et al., 2019; Yamamoto et al., 2004) and the manipulation of which affects *nkx2.1a* expression in vertebrates (including cavefish; Pabst et al., 2000; Rétaux et al., 2008), constitutes a likely candidate for this previously unreported phenotype. As Shh signalling during hypothalamus development controls the future numbers of specific peptidergic neuronal populations (Alié et al., 2018), it is tempting to hypothesize that these neuronal subsets might already be primed at tailbud stage. Lineage analyses should confirm these propositions.

rx3: an exemplary read-out of eye-field patterning and cell identity variations in cavefish

More striking than a systematic reduction of mRNA levels in cavefish, as described via transcriptomics (McGaugh et al., 2014; Julien Leclercq and S.R., unpublished), *rx3* expression is affected in many additional ways. Its domain of expression is smaller and is especially affected in the posterior part. This potentially explains the small size of early evaginating cavefish optic vesicles (Devos et al., 2021). Its fine regulation during co-expression with other transcription factors is modified at the eye-field boundaries (see above), with possible consequences for cell identities. Even more striking, *rx3* expression is always heterogeneous at the cell population level, a phenotype that is never observed for the other transcription factors studied: *pax6a*, *zic1* and *lhx2*. In cavefish prospective retinas, *rx3* levels are not only reduced compared with surface fish, but are also variable and unpredictable, and most likely affect cell programs and behaviours differently in neighbouring cells in a given sample and between samples. Finally, this low and heterogeneous cell level *rx3* expression could potentially affect expression of downstream eye-field effector molecules (Stigloher et al., 2006; Yin et al., 2014), as suggested by increased proportions of cells with medium *rx3* levels and high *cxcr4b* levels in cavefish. These quantifications in the natural cavefish mutant suggest a more-complex epistasis between *rx3* and *cxcr4* genes than previously described and/or additional regulatory modes. In zebrafish, *rx3*-dependent *cxcr4a* expression demarcates the telencephalic border of the eye field and confers specific segregative properties to the eye field at the onset of neurulation (Bielen and Houart, 2012). In cavefish, *rx3*-dependent *cxcr4b* regulation might also affect adhesive or migratory properties of optic cells during early eye evagination, as observed through live imaging (Devos et al., 2021).

We propose that the different aspects of *rx3* dysregulation have distinct developmental and genetic origins. The size of the *rx3* expression domain would be a 'simple' consequence of the many signalling modifications that have been described in cavefish during and at the end of gastrulation (Hh, Fgf, Bmp and Wnt: Hinaux et al., 2016; Pottin et al., 2011; Ren et al., 2018; Torres-Paz et al., 2019; Yamamoto et al., 2004). The *rx3* expression levels, on the other hand, and mostly its heterogeneity aspect, would probably result from intrinsic *cis*-regulatory changes at the level of the *rx3* locus.

In zebrafish, medaka and *Astyanax* surface fish, the paired-type homeodomain transcription factor *rx3* is crucial for eye development, as all *rx3* mutant fish are eyeless (Kennedy et al., 2004; Loosli et al., 2003, 2001; Warren et al., 2021). In these species, *rx3* controls survival of eye progenitors (Kennedy et al., 2004) as well as optic vesicle evagination and neuronal differentiation (Loosli et al., 2003), as revealed in the zebrafish *chokh/rx3* loss-of-function background. In cavefish, the optic vesicles and eyes formed are always smaller than in surface fish

and very little, if any, compensatory growth is observed (Devos et al., 2021), which contrasts with the *tcf7l1a* mutant embryos (Young et al., 2019). In the cavefish morph, no major apoptosis is recorded in optic vesicle cells during morphogenesis (Devos et al., 2021), and retinal apoptosis starts later, around 36-48 hpf (Alunni et al., 2007), in a lens-dependent manner (Yamamoto and Jeffery, 2000). It is possible that low and heterogeneous levels of *rx3* could allow cavefish optic cells to survive and might prime them for future apoptotic programs. At the tissue level, *rx3* heterogeneity may thus participate in a potential mechanism that allows progressive and controlled degeneration.

Heterochronic cavefish
Our study reveals substantial and more-subtle intra-species ANP differences, both in terms of eye-field regionalization/subdomains and at the single cell level. It also reveals striking differences in terms of apparent tissue dynamics: although some extent of eye-field condensation seems to occur at the onset of neurulation in surface fish, this global process of size reduction does not seem to take place in cavefish.

We developed a method of anterior ANP curvature normalization to allow the comparison of eye-field domain shape and size at similar stages of neural development. This uncovered two heterochronic processes in cavefish: a more advanced ANP curvature and a more anterior position of the prospective hypothalamus, which are likely to be uncorrelated. Importantly, the observed patterning differences were not subject to timing (i.e. they were observed for all d factors and were not delayed) and thus did not depend on neurulation advancement and keel formation.

In zebrafish, during the initial step of optic vesicle evagination, some eye-fated cells behave like the nearby telencephalic cells and converge towards the midline to form the neural keel, while others lag behind and keep the eye field wide (Ivanovitch et al., 2013; Rembold et al., 2006; reviewed by Bazin-Lopez et al., 2015; Sinn and Wittbrodt, 2013; Wilson and Houart, 2004). This midline convergence may underlie the decrease in volume specifically observed in surface fish for several markers, as a function of the d factor. Such predicted neural plate condensation is likely to take place over a short period in surface fish (<30 min) and may rely on intrinsic tissue properties that are impaired in cavefish, such as heterogeneous *rx3* expression and/or dysregulation of *cxcr4*, which normally influence the cohesion of eye-field cells (Bazin-Lopez et al., 2015).

Conclusions
All new ANP subdivisions found in *Astyanax* are likely present in other vertebrate species (Fig. 8). Detailed fate maps, lineage analyses and pseudo-time single-cell transcriptomics analyses will decipher their respective identities and outcomes. Intra-species differences observed here help to formulate hypotheses regarding the genetic specification of optic tissues, suggesting a substantial degree of variations between species. ANP phenotypes will guide the identification of the genetic basis of cavefish eye defects.

MATERIALS AND METHODS
A. mexicanus embryos
Our surface fish colony originates from rivers in Texas (USA) and our cavefish colony is derived from the Pachón cave in the state of Tamaulipas (Mexico). Embryos were obtained by *in vitro* fertilization, after induction of the breeding colony for gamete maturation and reproduction by changing the water temperature (Elipot et al., 2014). The embryonic development of

A. mexicanus at 24°C is similar and synchronous for both morphotypes (Hinaux et al., 2011).

Animals were treated according to French and European regulations of animals in research. S.R.'s authorization for the use of animals in research is 91-116. The protocol did not require authorization from the Paris Centre-Sud Ethic committee, as all experiments were performed on early [10 hpf (hours post-fertilization)] embryos, which are non-autonomous and have no nervous system.

Embryo staging and fixation

Morphological criteria were taken to stage 10 hpf and 10.5 hpf embryos, in addition to their known developmental time. These included extent of blastopore closure (100% epiboly), the prominent tail bud and the lateral flat triangular shape of the ANP (Hinaux et al., 2011). Embryos were fixed in 4% paraformaldehyde in PBS, dehydrated in graded ethanol/PBS steps and stored in methanol at −20°C.

Whole-mount *in situ* hybridization

Whole-mount *in situ* hybridization was carried out as previously described (Alié et al., 2018). Digoxigenin- and fluorescein-labelled riboprobes were prepared using PCR products as templates. cDNAs of interest were searched in our EST (expressed sequence tag) library (Hinaux et al., 2013). Clones in the library (pCMV SPORT6 vector) were: *rx3* (FO289986), *cxcr4b* (ARA0AAA96YA18), *pax6a* (ARA0AAA41YH22), *barhl2* (ARA0AEA6YL01), *nkx2.1a* (AY661435; Menuet et al., 2007), *zic1* (FO290256) (Devos et al., 2021), *lhx2* (EF175737) (Pottin et al., 2011), *emx3* (FO263072) and *dlx3b* (Hinaux et al., 2016). For fluorescent *in situ* visualization, FITC- and Cy3-tyramides (excitation peaks at 491 and 555 nm and emission peaks at 516 and 569 nm, respectively) were prepared as described previously (Zhou and Vize, 2004). Embryo were incubated in PBS containing 10 µM DAPI and 1% DMSO 24 h before dissection to stain nuclei, and washed in PBS.

Colorimetric *in situ* hybridization and image acquisition

Whole-mount embryos stained using colorimetric *in situ* hybridization were imaged on a Nikon AZ100 multizoom macroscope coupled to a Nikon digital sight DS-Ri1 camera, using the NIS software.

Fluorescent *in situ* hybridization and neural plate dissections

Fluorescently labelled embryos were transferred to a Sylgard-containing Petri dish bathed in PBT (PBS+0.3% Tween). Embryos were cut using forceps (Fine Science Tools, 5 Ultra) into two pieces at the yolk equator. After yolk removal, green and/or red staining of the ANP served to dissect out and isolate a piece of tissue containing the labelled ANP, under a fluorescent dissecting microscope. Dissected ANP were mounted in dorsal views in Vectashield (Vector) between glass slides and coverslips inside wells built with one reinforcement ring to limit neuro-ectodermal tissue flattening.

Fluorescent image stack acquisition

Confocal image stacks were captured on a confocal Leica SP8 microscope using the Leica Application Suite software. Water immersion objective (HC FLUOTAR L 25×/0.95 W VISIR 2.50 Water) was used for all experiments except for 'single cell' analyses, which required a 40× objective (HC PL APO 40×/1.10 W CORR CS2 0.65 Water 0.14–0.18) to improve resolution and hence better separate nuclei pixel intensities. As we did not compare mean intensities between samples but relative fluorescent levels within each normalized sample, we chose the optimal laser power and photo-multiplicator gain (PMT, ranging from 450 V to 630 V) for each sample acquisition. PMT gain compensation in the *z*-axis was also applied to capture signals in ventral deeper regions when stacking the entire eye field. Acquisitions were performed using sequential modes with optimization of emission wavelength range to avoid bleed-through of signals. Image stacks depth of entire neural plate typically ranged between 70 and 90 *z* steps depending on samples. A *z* step of 1 µm was used for each confocal acquisition. Image size and format were of 512×512 pixels and 8 bit, respectively.

Neural plate staging: d factor

The anterior curvature of the ANP looks like a parabola ($y=ax^2$), where (a) corresponds to the vertical scaling factor. For convenience of our experimental design we used the formula ($y=x^2/d$), where factor d is the inverse of a. Therefore, the higher d is, the flatter the curve of the ANP is and the less advanced convergence is. Conversely, a lower d factor indicates a strong curvature of the ANP and thus advanced tissue convergence. We generated a single image (512×512 pixels) containing a merge of nine parabolas ranging from d factors 1 to 9, in an orthonormal system (Fig. 1I-I‴). This allowed us to generate composite 2-channel images containing a maximum intensity projection of single fluorescent *in situ* hybridization image stacks superimposed on the parabolas grid, in which the ANR medial anterior point was positioned at ($x=0$, $y=0$). We then assessed to which parabola/d factor each sample was best fitted (by eye). As ANP anterior curvatures were sometimes slightly asymmetric, we calculated the d factor for each sample as the mean of the two values estimated for the left and right side. We validated the accuracy of this method by merging images of similar d factors and controlling their shape correspondence (by eye). Overall, this method allowed the assessment of intrinsic neural temporality and staging for each sample, and compared them according to this criterion.

Morphometric analyses

All images were obtained from flat-mount dissected ANP (except for Fig. 1A,B).

2D and 3D size analyses

Size areas on colorimetric and fluorescence images were measured by tracing contours manually using FIJI (Schindelin et al., 2012). Volumes on image stacks were calculated as follows: for each marker, objects were generated after segmentation with Imaris software (Bitplane) using a common method (the same threshold method and morphological filters). For each channel, we created a corresponding cell using the default mode (settings: volume display). Cell body detection used the smooth option (filter width 2 µm). Cell threshold (absolute intensity) did not split touching cells and was adapted for each sample. Object properties were thereafter extracted (i.e. volumes). To compute the volume of the overlapping region between two markers, we used the 'Surface-surface colocalization XTension' (Imaris).

For Fig. 5, the volume of the domain expressing only *rx3* (*zic1⁻*) was calculated by adding the areas of binarized objects at each plan. For Fig. 4E, we used the measure stack plug-in (FIJI), which allows the semi-automatic drawing of *nkx2.1a* domain contours in each *z* step, the sum of which allowed the calculation of the volume of prospective hypothalamus.

For Fig. 5D,E and Movie 7, we applied the Make Binary plug-in (FIJI) on image stacks, setting identical minimum and maximum pixel intensities for all samples compared. Symmetrical subtraction of binarized *zic1* and *rx3* stack channels using the Image Calculator plug-in allowed the generation of $zic1^+/rx3^-$ and $rx3^+/zic1^-$ images. Segmented areas were calculated from maximum pixel intensity ventral half-stack projections using the Wand Tool. Volume of the midline ventral $rx3^+/zic1^-$ domain was calculated by summing all *z* segmented areas from *rx3/zic1* subtracted images.

2D and 3D rendering

We performed volume rendering using the 3D Viewer plug-in (FIJI) and Imaris (see figure legends).

Image processing and analyses

All maximum projections were performed on raw image stacks. Fluorescence signals were measured on maximum intensity projections, the contrasts of which were adjusted automatically, in order to optimize the dynamic range of pixel intensities. Background signals were removed for each image by subtracting the average pixel intensity measured for each marker outside the ROI and all fluorescence levels were then normalized by the maximum value of the image. For Figs 1–7, images were adjusted for brightness and contrast, with no other modifications. For Fig. 3 and Fig. S8, the *barhl2/pax6a* and *nkx2.1a/pax6a* images were cropped to show only the ANP (because of high unaesthetic background signal in anterior non-neural

ectoderm). All images of the ANP show anterior towards the top except for Fig. 1I-I‴ (towards the bottom).

Plot profiles

We generated plot profiles from maximum intensity projections of 10 µm sections at a position close to mid-*z*-depth of the expression domains considered in the majority of the experiments. For Figs 4, 6 and Figs S9 and S10, maximum intensity projections corresponded to entire stacks. In Fig. 4, we considered this variant for measurement as it clearly showed the relative position of the two tissues: eye field and prospective hypothalamus. For Fig. 6, it reflected well the relative position of the pairs of markers considered in the bended prospective telencephalon. The ROIs selected for measurements are indicated in each figure. Owing to inter-individual size differences, the length of each plot for *rx3* (Fig. 1), *pax6a/rx3* (Fig. 3) and *nkx2.1a/rx3* (Fig. 4) was normalized by the total distance, thus allowing inter-sample relative pixel intensity comparisons. For specific analyses at domain boundaries, the ROIs for *pax6a/barhl2* (Fig. 2), *emx3/zic1* and *zic1/rx3* (Fig. 7) were 20 µm wide and 50 µm long.

For analyses in the D/V axis (Fig. 3), we resliced image stacks entirely according to the indicated scheme to generate 3 µm sagittal projections. We next quantified relative pixel intensities in D/V line histograms equally spaced in the A/P axis inside the *rx3* domain.

Plot profiles averaging

In order to compare normalized pixel intensities within the same relative zone between samples of different sizes, we averaged intensity values within intervals of 0.02 or 0.05 in the *x* axis.

Single cell analyses

For individual cell fluorescence quantifications, we used 2 µm maximum intensity projection images. Nuclear staining (DAPI) served to segment 'individual particles' in the ROI, allowing measurement of pixel intensity mean levels for all channels (single cells). As shown in Fig. S1, fluorescence levels measured in individual nuclei areas reflected the fluorescence levels in the corresponding surrounding concentric zones, thus showing that measuring pixel intensity levels in the nuclear zones was a good proxy of individual cell fluorescence levels. Again, as all fluorescence measurements were normalized, this allowed the comparison of relative fluorescent intensity levels – taken as a proxy of gene expression level – between cells within a given sample.

Statistical analyses

Mann-Whitney *U*-tests were used in Fig. 1K-N,R,V, Fig. 2H,K,L, Fig. 3I-L, Fig. 4E,G, Fig. 5F-J, Fig. 6E,F,H,I and Fig. 7C. *P* values are indicated in respective figures. A two-sided *t*-test with unequal variance was used for Fig. 5A″. Spearman correlation was used and R coefficient calculated in Figs 1P and 6J. Two-way ANOVA tests were used for Fig. 1Q,U, Fig. 3F,H,P, Fig. 4F, Fig. 5C, Fig. 6Q and Fig. 7E. Black bars and asterisks indicate significant differences. Chi-squared tests were performed in Fig. 2M, Fig. 4L and Fig. 7H. *P* value are indicated in each figure. Fisher's exact test was performed in Fig. 6U,W, *P* values are indicated at the bottom. No statistical method was used to predetermine sample size. All experiments shown were replicated at least twice. The experiments were not randomized and the investigators were not blinded to allocation during experiments and outcome assessment.

Competing interests

The authors declare no competing or financial interests.

Author contributions

Conceptualization: F.A., J.T.-P., S.R.; Methodology: F.A., J.T.-P., S.R.; Validation: F.A., J.T.-P.; Formal analysis: F.A., J.T.-P.; Investigation: F.A., J.T.-P., P.M.; Resources: F.A., J.T.-P., S.R.; Writing - original draft: F.A., J.T.-P., S.R.; Writing - review & editing: F.A., J.T.-P., S.R.; Visualization: F.A., J.T.-P.; Supervision: S.R.; Project administration: S.R.; Funding acquisition: S.R.

Peer review history

The peer review history is available online at https://journals.biologists.com/dev/article-lookup/doi/10.1242/dev.199966.

References

Affaticati, P., Yamamoto, K., Rizzi, B., Bureau, C., Peyriéras, N., Pasqualini, C., Demarque, M. and Vernier, P. (2015). Identification of the optic recess region as a morphogenetic entity in the zebrafish forebrain. *Sci. Rep.* **5**, 8738. doi:10.1038/srep08738

Alié, A., Devos, L., Torres-Paz, J., Prunier, L., Boulet, F., Blin, M., Elipot, Y. and Retaux, S. (2018). Developmental evolution of the forebrain in cavefish, from natural variations in neuropeptides to behavior. *eLife* **7**, e32808. doi:10.7554/eLife.32808

Alunni, A., Menuet, A., Candal, E., Penigault, J.-B., Jeffery, W. R. and Rétaux, S. (2007). Developmental mechanisms for retinal degeneration in the blind cavefish Astyanax mexicanus. *J. Comp. Neurol.* **505**, 221-233. doi:10.1002/cne.21488

Bazin-Lopez, N., Valdivia, L. E., Wilson, S. W. and Gestri, G. (2015). Watching eyes take shape. *Curr. Opin. Genet. Dev.* **32**, 73-79. doi:10.1016/j.gde.2015.02.004

Bielen, H. and Houart, C. (2012). BMP signaling protects telencephalic fate by repressing eye identity and its Cxcr4-dependent morphogenesis. *Dev. Cell* **23**, 812-822. doi:10.1016/j.devcel.2012.09.006

Bielen, H., Pal, S., Tole, S. and Houart, C. (2017). Temporal variations in early developmental decisions: an engine of forebrain evolution. *Curr. Opin. Neurobiol.* **42**, 152-159. doi:10.1016/j.conb.2016.12.008

Cavodeassi, F. and Houart, C. (2012). Brain regionalization: of signaling centers and boundaries. *Dev. Neurobiol.* **72**, 218-233. doi:10.1002/dneu.20938

Devos, L., Agnès, F., Edouard, J., Simon, V., Legendre, L., Elkhallouki, N., Barbachou, S., Sohm, F. and Rétaux, S. (2021). Eye morphogenesis in the blind Mexican cavefish. *Biol. Open* **10**, bio059031. doi:10.1242/bio.059031

Elipot, Y., Legendre, L., Père, S., Sohm, F. and Rétaux, S. (2014). Astyanax transgenesis and husbandry: how cavefish enters the laboratory. *Zebrafish* **11**, 291-299. doi:10.1089/zeb.2014.1005

England, S. J., Blanchard, G. B., Mahadevan, L. and Adams, R. J. (2006). A dynamic fate map of the forebrain shows how vertebrate eyes form and explains two causes of cyclopia. *Development* **133**, 4613-4617. doi:10.1242/dev.02678

Fish, M. B., Nakayama, T., Fisher, M., Hirsch, N., Cox, A., Reeder, R., Carruthers, S., Hall, A., Stemple, D. L. and Grainger, R. M. (2004). Xenopus mutant reveals necessity of rax for specifying the eye field which otherwise forms tissue with telencephalic and diencephalic character. *Dev. Biol.* **395**, 317-330. doi:10.1016/j.ydbio.2014.09.004

Gehring, W. J. (1996). The master control gene for morphogenesis and evolution of the eye. *Genes Cells* **1**, 11-15. doi:10.1046/j.1365-2443.1996.11011.x

Giger, F. A. and Houart, C. (2018). The birth of the eye vesicle: when fate decision equals morphogenesis. *Front. Neurosci.* **12**, 87. doi:10.3389/fnins.2018.00087

Grinblat, Y., Gamse, J., Patel, M. and Sive, H. (1998). Determination of the zebrafish forebrain: induction and patterning. *Development* **125**, 4403-4416. doi:10.1242/dev.125.22.4403

Heisenberg, C.-P., Houart, C., Take-Uchi, M., Rauch, G.-J., Young, N., Coutinho, P., Masai, I., Caneparo, L., Concha, M. L., Geisler, R. et al. (2001). A mutation in the Gsk3-binding domain of zebrafish Masterblind/Axin1 leads to a fate transformation of telencephalon and eyes to diencephalon. *Genes Dev.* **15**, 1427-1434. doi:10.1101/gad.194301

Hinaux, H., Pottin, K., Chalhoub, H., Père, S., Elipot, Y., Legendre, L. and Rétaux, S. (2011). A developmental staging table for Astyanax mexicanus surface fish and Pachon cavefish. *Zebrafish* **8**, 155-165. doi:10.1089/zeb.2011.0713

Hinaux, H., Poulain, J., Da Silva, C., Noirot, C., Jeffery, W. R., Casane, D. and Rétaux, S. (2013). De novo sequencing of astyanax mexicanus surface fish and Pachón cavefish transcriptomes reveals enrichment of mutations in cavefish putative eye genes. *PLoS ONE* **8**, e53553. doi:10.1371/journal.pone.0053553

DEVELOPMENT

13

Hinaux, H., Devos, L., Bibliowicz, J., Elipot, Y., Alié, A., Blin, M. and Rétaux, S. (2016). Sensory evolution in blind cavefish is driven by early embryonic events during gastrulation and neurulation. *Development* **143**, 4521-4532. doi:10.1242/dev.141291

Houart, C., Westerfield, M. and Wilson, S. W. (1998). A small population of anterior cells patterns the forebrain during zebrafish gastrulation. *Nature* **391**, 788-792. doi:10.1038/35853

Houart, C., Caneparo, L., Heisenberg, C.-P., Barth, K. A., Take-Uchi, M. and Wilson, S. W. (2002). Establishment of the telencephalon during gastrulation by local antagonism of Wnt signaling. *Neuron* **35**, 255-265. doi:10.1016/S0896-6273(02)00751-1

Ivanovitch, K., Cavodeassi, F. and Wilson, S. W. (2013). Precocious acquisition of neuroepithelial character in the eye field underlies the onset of eye morphogenesis. *Dev. Cell* **27**, 293-305. doi:10.1016/j.devcel.2013.09.023

Kennedy, B. N., Stearns, G. W., Smyth, V. A., Ramamurthy, V., van Eeden, F., Ankoudinova, I., Raible, D., Hurley, J. B. and Brockerhoff, S. E. (2004). Zebrafish rx3 and mab21l2 are required during eye morphogenesis. *Dev. Biol.* **270**, 336-349. doi:10.1016/j.ydbio.2004.02.026

Kwan, K. M., Otsuna, H., Kidokoro, H., Carney, K. R., Saijoh, Y. and Chien, C.-B. (2012). A complex choreography of cell movements shapes the vertebrate eye. *Development* **139**, 359-372. doi:10.1242/dev.071407

Loosli, F., Winkler, S., Burgtorf, C., Wurmbach, E., Ansorge, W., Henrich, T., Grabher, C., Arendt, D., Carl, M., Krone, A. et al. (2001). Medaka eyeless is the key factor linking retinal determination and eye growth. *Development* **128**, 4035-4044. doi:10.1242/dev.128.20.4035

Loosli, F., Staub, W., Finger-Baier, K. C., Ober, E. A., Verkade, H., Wittbrodt, J. and Baier, H. (2003). Loss of eyes in zebrafish caused by mutation of chokh/rx3. *EMBO Rep.* **4**, 894-899. doi:10.1038/sj.embor.embor919

Macdonald, R., Xu, Q., Barth, K. A., Mikkola, I., Holder, N., Fjose, A., Krauss, S. and Wilson, S. W. (1994). Regulatory gene expression boundaries demarcate sites of neuronal differentiation in the embryonic zebrafish forebrain. *Neuron* **13**, 1039-1053. doi:10.1016/0896-6273(94)90044-2

Macdonald, R., Scholes, J., Strahle, U., Brennan, C., Holder, N., Brand, M. and Wilson, S. W. (1997). The Pax protein Noi is required for commissural axon pathway formation in the rostral forebrain. *Development* **124**, 2397-2408. doi:10.1242/dev.124.12.2397

Maurus, D. and Harris, W. A. (2009). Zic-associated holoprosencephaly: zebrafish Zic1 controls midline formation and forebrain patterning by regulating Nodal, Hedgehog, and retinoic acid signaling. *Genes Dev.* **23**, 1461-1473. doi:10.1101/gad.517009

McGaugh, S. E., Gross, J. B., Aken, B., Blin, M., Borowsky, R., Chalopin, D., Hinaux, H., Jeffery, W. R., Keene, A., Ma, L. et al. (2014). The cavefish genome reveals candidate genes for eye loss. *Nat. Commun.* **5**, 5307. doi:10.1038/ncomms6307

Menuet, A., Alunni, A., Joly, J.-S., Jeffery, W. R. and Rétaux, S. (2007). Expanded expression of Sonic Hedgehog in Astyanax cavefish: multiple consequences on forebrain development and evolution. *Development* **134**, 845-855. doi:10.1242/dev.02780

Morita, T., Nitta, H., Kiyama, Y., Mori, H. and Mishina, M. (1995). Differential expression of two zebrafish emx homeoprotein mRNAs in the developing brain. *Neurosci. Lett.* **198**, 131-134. doi:10.1016/0304-3940(95)11988-9

Muthu, V., Eachus, H., Ellis, P., Brown, S. and Placzek, M. (2016). Rx3 and Shh direct anisotropic growth and specification in the zebrafish tuberal/anterior hypothalamus. *Development* **143**, 2651-2663. doi:10.1242/dev.138305

Orquera, D. P. and de Souza, F. S. J. (2016). Evolution of the Rax family of developmental transcription factors in vertebrates. *Mech. Dev.* **144**, 163-170. doi:10.1016/j.mod.2016.11.002

Pabst, O., Herbrand, H., Takuma, N. and Arnold, H.-H. (2000). NKX2 gene expression in neuroectoderm but not in mesendodermally derived structures depends on sonic hedgehog in mouse embryos. *Dev. Genes Evol.* **210**, 47-50. doi:10.1007/PL00008188

Porter, F. D., Drago, J., Xu, Y., Cheema, S. S., Wassif, C., Huang, S. P., Lee, E., Grinberg, A., Massalas, J. S., Bodine, D. et al. (1997). Lhx2, a LIM homeobox gene, is required for eye, forebrain, and definitive erythrocyte development. *Development* **124**, 2935-2944. doi:10.1242/dev.124.15.2935

Pottin, K., Hinaux, H. and Rétaux, S. (2011). Restoring eye size in Astyanax mexicanus blind cavefish embryos through modulation of the Shh and Fgf8 forebrain organising centres. *Development* **138**, 2467-2476. doi:10.1242/dev.054106

Rembold, M., Loosli, F., Adams, R. J. and Wittbrodt, J. (2006). Individual cell migration serves as the driving force for optic vesicle evagination. *Science* **313**, 1130-1134. doi:10.1126/science.1127144

Ren, X., Hamilton, N., Müller, F. and Yamamoto, Y. (2018). Cellular rearrangement of the prechordal plate contributes to eye degeneration in the cavefish. *Dev. Biol.* **441**, 221-234. doi:10.1016/j.ydbio.2018.07.017

Rétaux, S., Pottin, K. and Alunni, A. (2008). Shh and forebrain evolution in the blind cavefish Astyanax mexicanus. *Biol. Cell* **100**, 139-147. doi:10.1042/BC20070084

Rétaux, S., Bourrat, F., Joly, J. and Hinaux, H. (2013). Perspectives in Evo-Devo of the vertebrate brain. In *Advances in Evolutionary Developmental Biology*, 1st edn. (ed. J. Todd Streelman), pp. 151-172. John Wiley & Sons, Inc.

Rétaux, S., Alié, A., Blin, M., Devos, L., Elipot, Y. and Hinaux, H. (2016). Neural development and evolution in Astyanax mexicanus: comparing cavefish and surface fish brains. In *Biology and Evolution of the Mexican Cavefish. Chapter 12* (ed. A. C. Keen, M. Yoshizawa and S. E. McGaugh), pp. 223-240. Elsevier, Academic Press.

Rubenstein, J. L. R., Shimamura, K., Martinez, S. and Puelles, L. (1998). Regionalization of the prosencephalic neural plate. *Annu. Rev. Neurosci.* **21**, 445-477. doi:10.1146/annurev.neuro.21.1.445

Schindelin, J., Arganda-Carreras, I., Frise, E., Kaynig, V., Longair, M., Pietzsch, T., Preibisch, S., Rueden, C., Saalfeld, S., Schmid, B. et al. (2012). Fiji: an open-source platform for biological-image analysis. *Nat. Methods* **9**, 676-682. doi:10.1038/nmeth.2019

Sinn, R. and Wittbrodt, J. (2013). An eye on eye development. *Mech. Dev.* **130**, 347-358. doi:10.1016/j.mod.2013.05.001

Staudt, N. and Houart, C. (2007). The prethalamus is established during gastrulation and influences diencephalic regionalization. *PLoS Biol.* **5**, e69. doi:10.1371/journal.pbio.0050069

Staudt, N., Giger, F. A., Fielding, T., Hutt, J. A., Foucher, I., Snowden, V., Hellich, A., Kiecker, C. and Houart, C. (2019). Pineal progenitors originate from a non-neural territory limited by FGF signalling. *Development* **146**, dev171405. doi:10.1242/dev.171405

Stigloher, C., Ninkovic, J., Laplante, M., Geling, A., Tannhäuser, B., Topp, S., Kikuta, H., Becker, T. S., Houart, C. and Bally-Cuif, L. (2006). Segregation of telencephalic and eye-field identities inside the zebrafish forebrain territory is controlled by Rx3. *Development* **133**, 2925-2935. doi:10.1242/dev.02450

Strickler, A. G., Yamamoto, Y. and Jeffery, W. R. (2001). Early and late changes in Pax6 expression accompany eye degeneration during cavefish development. *Dev. Genes Evol.* **211**, 138-144. doi:10.1007/s004270000123

Tessmar-Raible, K., Raible, F., Christodoulou, F., Guy, K., Rembold, M., Hausen, H. and Arendt, D. (2007). Conserved sensory-neurosecretory cell types in annelid and fish forebrain: insights into hypothalamus evolution. *Cell* **129**, 1389-1400. doi:10.1016/j.cell.2007.04.041

Toro, S. and Varga, Z. M. (2007). Equivalent progenitor cells in the zebrafish anterior preplacodal field give rise to adenohypophysis, lens, and olfactory placodes. *Semin. Cell Dev. Biol.* **18**, 534-542. doi:10.1016/j.semcdb.2007.04.003

Torres-Paz, J., Leclercq, J. and Rétaux, S. (2019). Maternally regulated gastrulation as a source of variation contributing to cavefish forebrain evolution. *eLife* **8**, e50160. doi:10.7554/eLife.50160

Varga, Z. M., Wegner, J. and Westerfield, M. (1999). Anterior movement of ventral diencephalic precursors separates the primordial eye field in the neural plate and requires cyclops. *Development* **126**, 5533-5546. doi:10.1242/dev.126.24.5533

Warren, W. C., Boggs, T. E., Borowsky, R., Carlson, B. M., Ferrufino, E., Gross, J. B., Hillier, L., Hu, Z., Keene, A. C., Kenzior, A. et al. (2021). A chromosome-level genome of Astyanax mexicanus surface fish for comparing population-specific genetic differences contributing to trait evolution. *Nat. Commun.* **12**, 1447. doi:10.1038/s41467-021-21733-z

Wilson, S. W. and Houart, C. (2004). Early steps in the development of the forebrain. *Dev. Cell* **6**, 167-181. doi:10.1016/S1534-5807(04)00027-9

Woo, K. and Fraser, S. E. (1995). Order and coherence in the fate map of the zebrafish nervous system. *Development* **121**, 2595-2609. doi:10.1242/dev.121.8.2595

Yamamoto, Y. and Jeffery, W. R. (2000). Central role for the lens in cave fish eye degeneration. *Science* **289**, 631-633. doi:10.1126/science.289.5479.631

Yamamoto, Y., Stock, D. W. and Jeffery, W. R. (2004). Hedgehog signalling controls eye degeneration in blind cavefish. *Nature* **431**, 844-847. doi:10.1038/nature02864

Yin, J., Morrissey, M. E., Shine, L., Kennedy, C., Higgins, D. G. and Kennedy, B. N. (2014). Genes and signaling networks regulated during zebrafish optic vesicle morphogenesis. *BMC Genomics* **15**, 825. doi:10.1186/1471-2164-15-825

Young, R. M., Hawkins, T. A., Cavodeassi, F., Stickney, H. L., Schwarz, Q., Lawrence, L. M., Wierzbicki, C., Cheng, B. Y. L., Luo, J., Ambrosio, E. M. et al. (2019). Compensatory growth renders Tcf7l1a dispensable for eye formation despite its requirement in eye field specification. *eLife* **8**, e40093. doi:10.7554/eLife.40093

Zhou, X. and Vize, P. D. (2004). Proximo-distal specialization of epithelial transport processes within the Xenopus pronephric kidney tubules. *Dev. Biol.* **271**, 322-338. doi:10.1016/j.ydbio.2004.03.036

Zuber, M. E., Gestri, G., Viczian, A. S., Barsacchi, G. and Harris, W. A. (2003). Specification of the vertebrate eye by a network of eye field transcription factors. *Development* **130**, 5155-5167. doi:10.1242/dev.00723

DEVELOPMENT
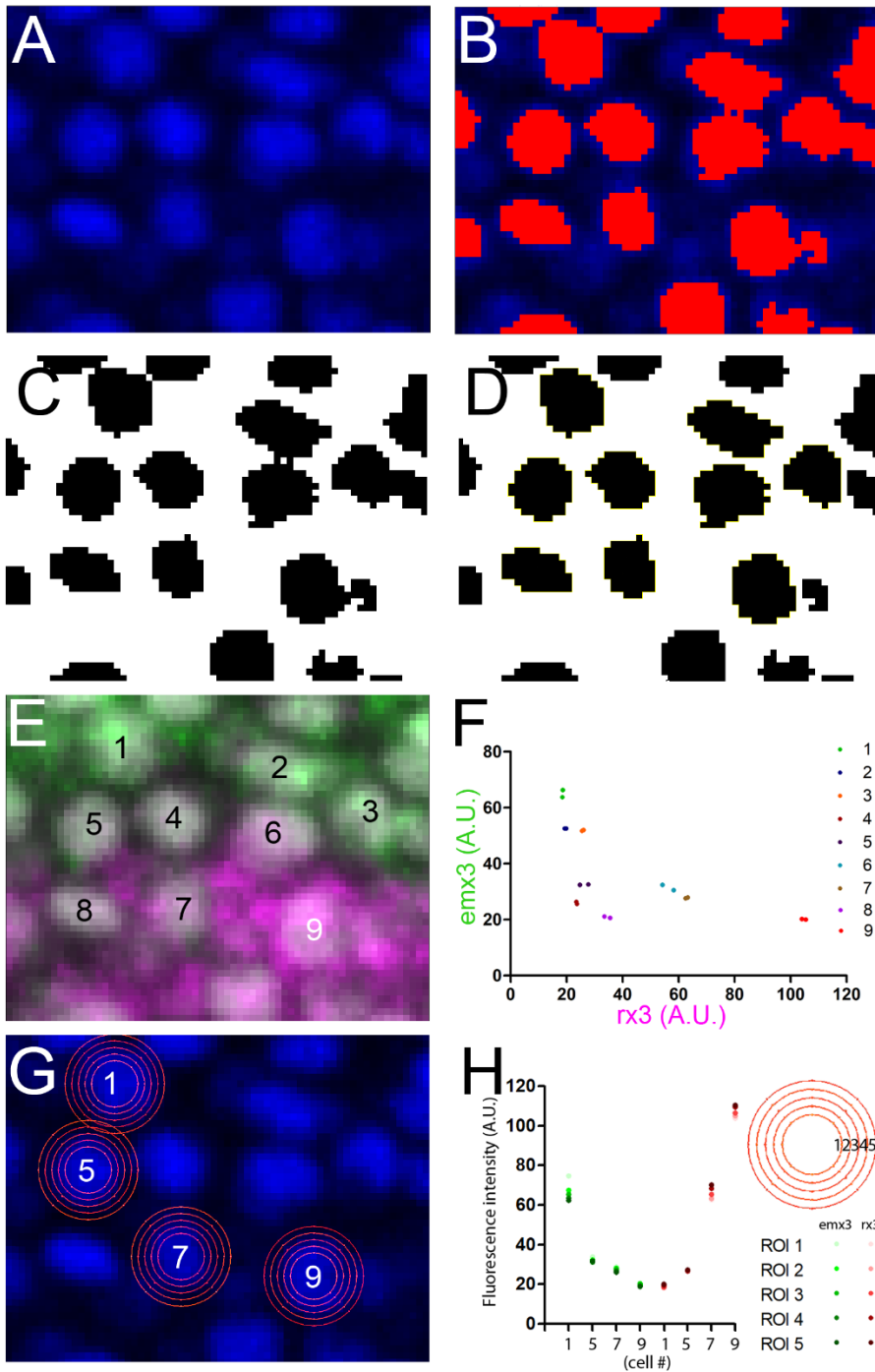
Fig. S1. Workflow for measurements of fluorescence levels in individual cells. (A) Nuclear staining with DAPI, 3μm section. (B) Thresholding of DAPI signal used for binarization. (C) Segmentation after thresholding. (D) Manual corrections after segmentation. (E) Expression of *emx3* (green) and *rx3* (magenta), individual cells are indicated with numbers. (F) Fluorescence levels in individual cells in duplicate measurements by segmentation using thresholding (A-D) and by manual segmentation. (G) Concentric ROIs of different sizes for measuring fluorescence levels. (H) Comparison of fluorescence levels measured by modifying the size of the ROI.
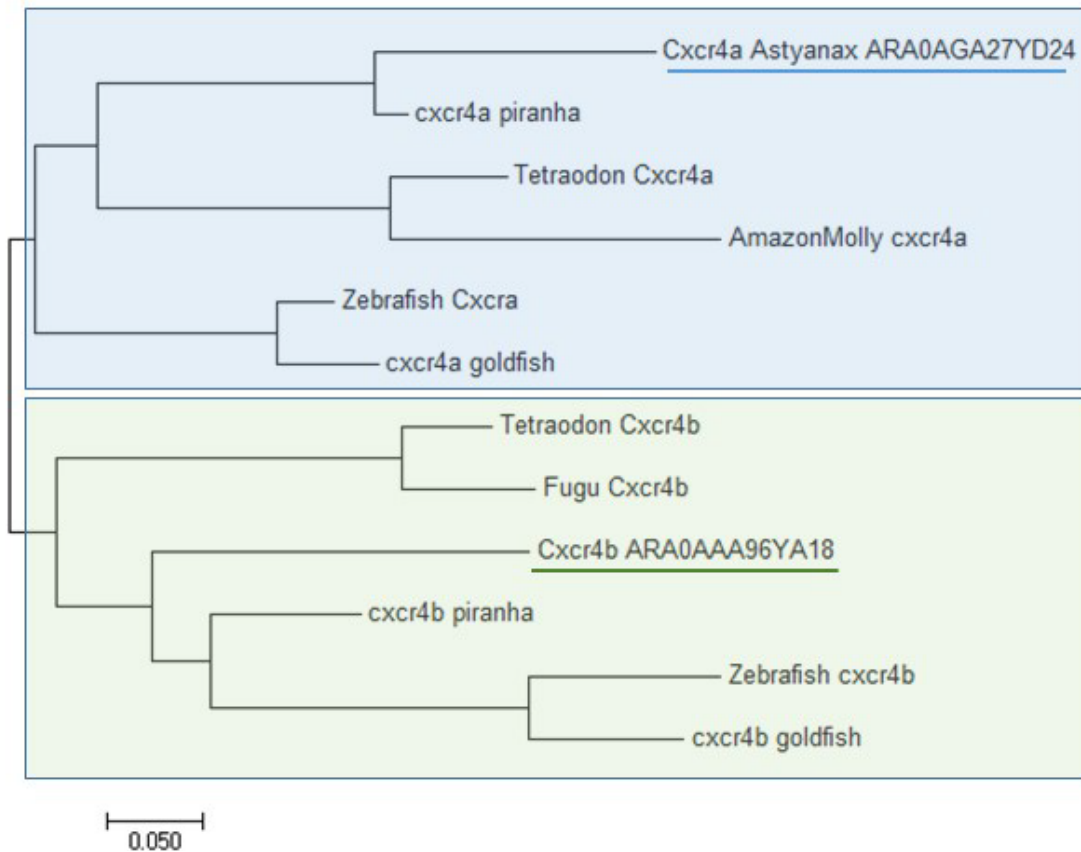
Fig. S2. Phylogenetic tree of fish Cxcr4a/b protein sequences. Maximum likelihood tree of fish Cxcr4a/b protein sequences. *Astyanax mexicanus* protein sequences (genome assembly) were deduced after sequencing of clones obtained from our cDNA library (underlined). We used *cxcr4b* in the present study.
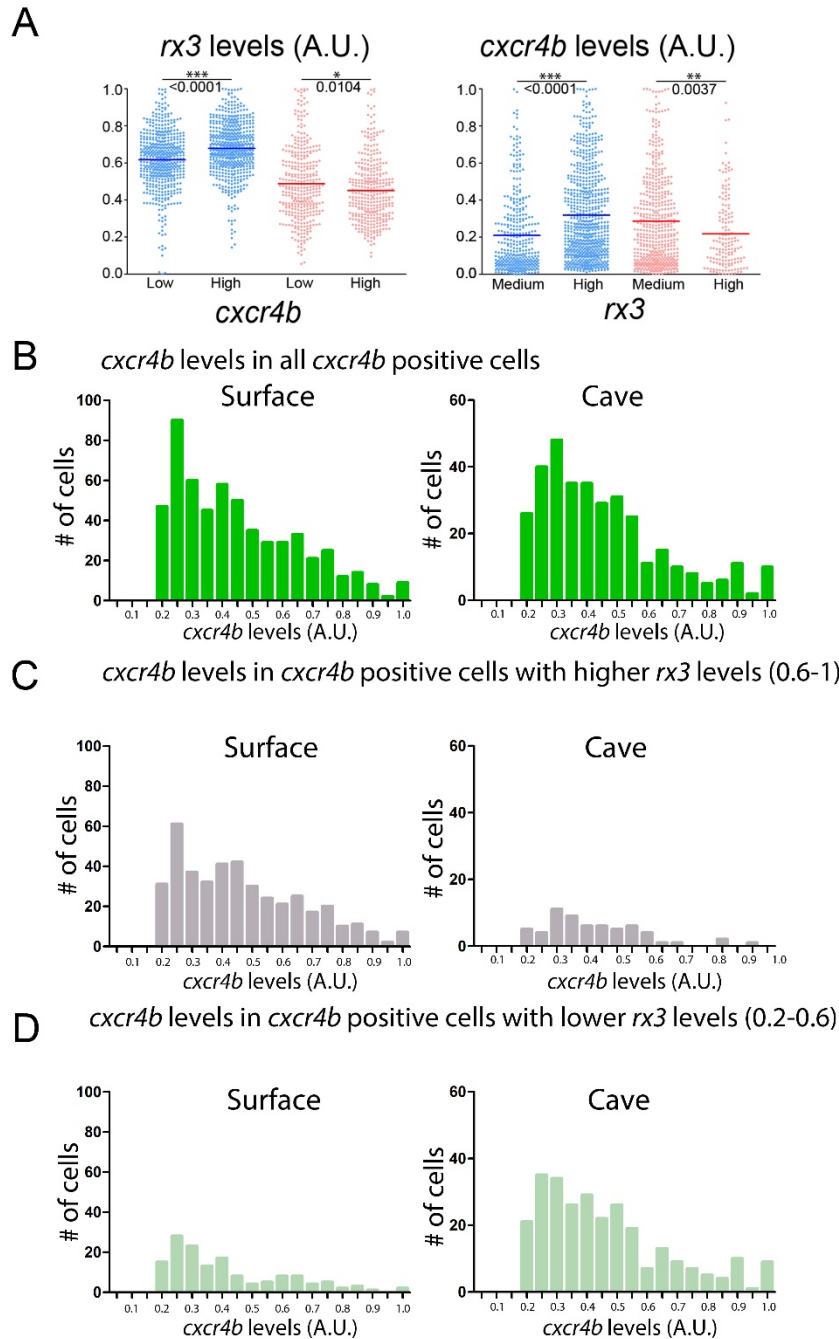
Fig. S3. Quantifications of *rx3* and *cxcr4b* levels. (A) *rx3* relative pixel intensity levels, according to low (0-0,2 AU) and higher (0.2-1 AU) *cxcr4b* levels (left) ; and *cxcr4b* relative pixel intensity levels, according to medium (0.2-0.6 AU) and high (0.6-1 AU) *rx3* levels (right), in surface fish (blue) and cavefish (red). Mean values are indicated by bars. Mann-Whitney test were performed. **(B-D)** Frequency histograms showing the distribution of cells according to different *cxcr4b* fluorescence levels (B), only for cells with high *rx3* levels (C), only for cells with lower *rx3* levels (D). All graphs correspond to ROI indicated in Figure 2I.
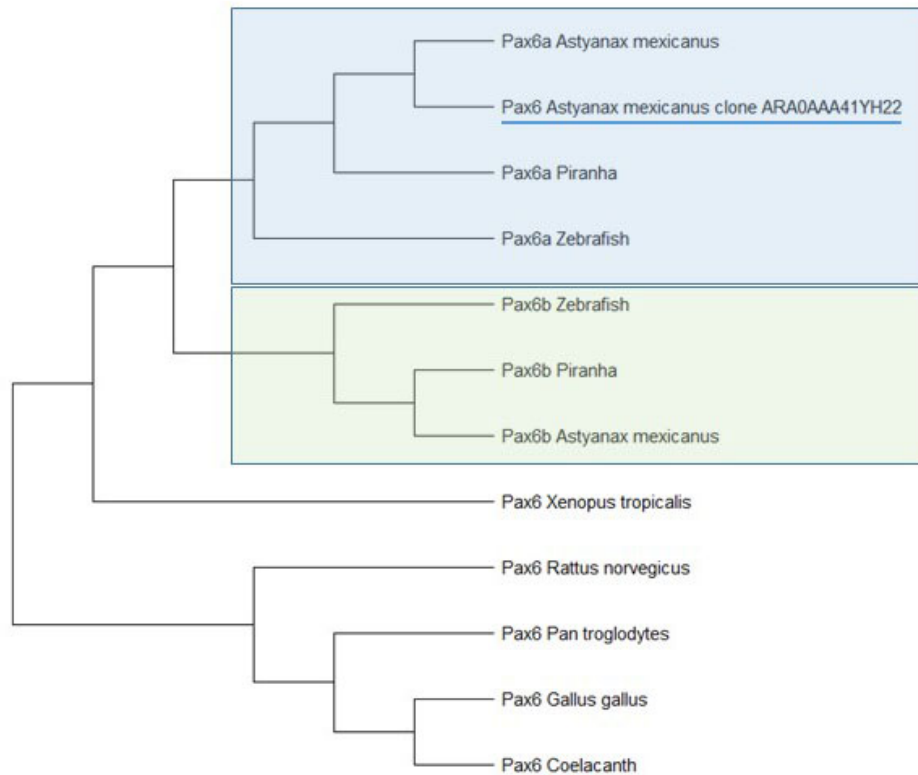
Fig. S4. Phylogenetic tree of fish Pax6a/b protein sequences. Neighbor-Joining bootstrap consensus tree on Pax6 protein alignments, performed in MEGA11. The translated protein (partial sequence, 155 amino acids) from the ARA0AAA41YH22 clone is 100% identical to the Genbank *Astyanax mexicanus pax6a* sequence.
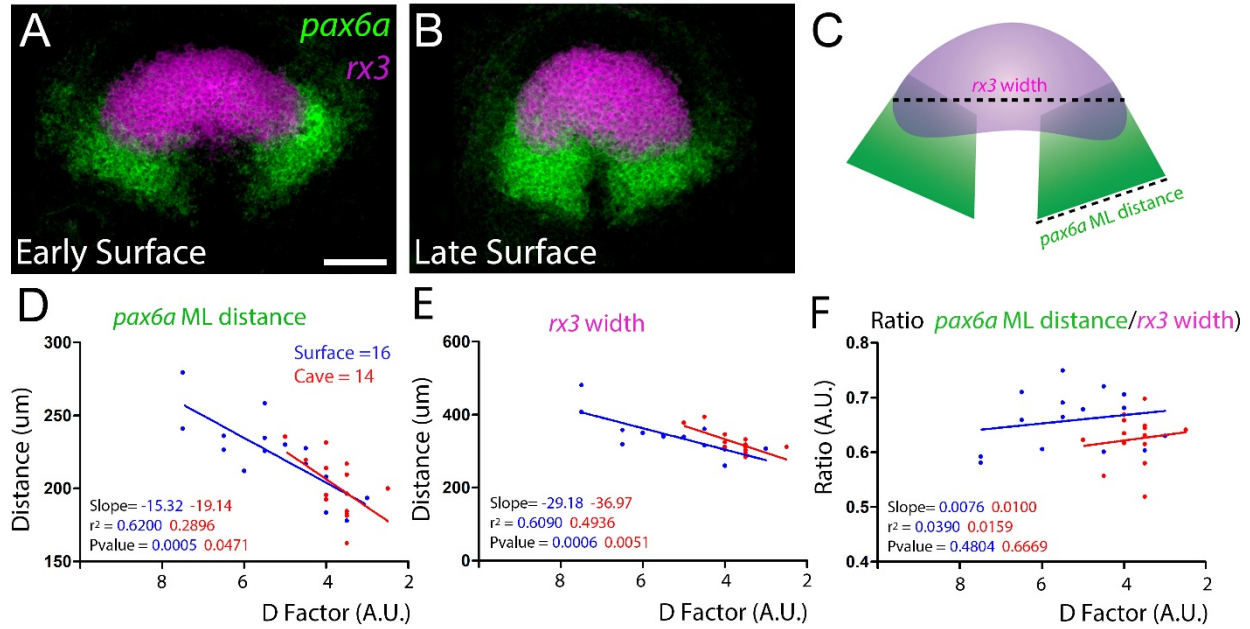
Fig. S5. Comparison of neurulation in cavefish and surface fish. (A-B) Maximum intensity projections shing the expression of *pax6a* and *rx3* in surface fish embryos at early and late neurulation states of the tailbud stage. Scheme indicating the distances measured in the *rx3* and *pax6a* expression domains. (D-F). Plots showing the pax6a ML distance (D), *rx3* width (E) and the ratio *pax6a* ML distance/*rx3* width (F) according to the different D factors. Linear regressions were calculated and the parameters obtained are indicated. Scale bar, 100µm.
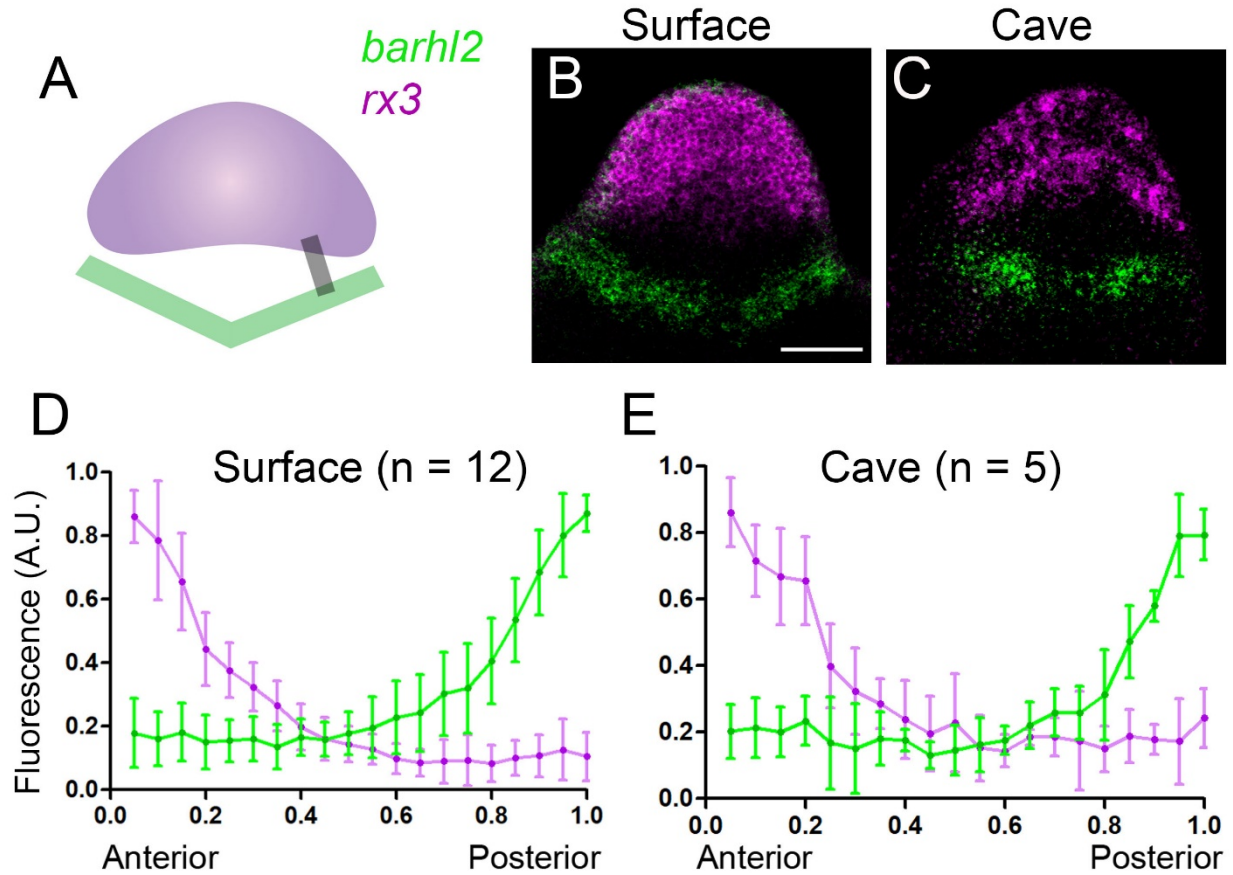
Fig. S6. Relative position of *barhl2* and *rx3* domains. (A) Scheme indicating the ROI measured covering posterior *rx3* to anterior *barhl2* domains. (B-C) Maximum intensity projections showing expression of *rx3* and *barhl2* in surface (B) and cavefish (C) embryos at 10hpf. (D-E) Fluorescence levels of *rx3* (magenta) and *barhl2* (green) according to line in (A) anterior to posterior in surface (D) and cavefish (E) embryos. Scale bar, 100μm.
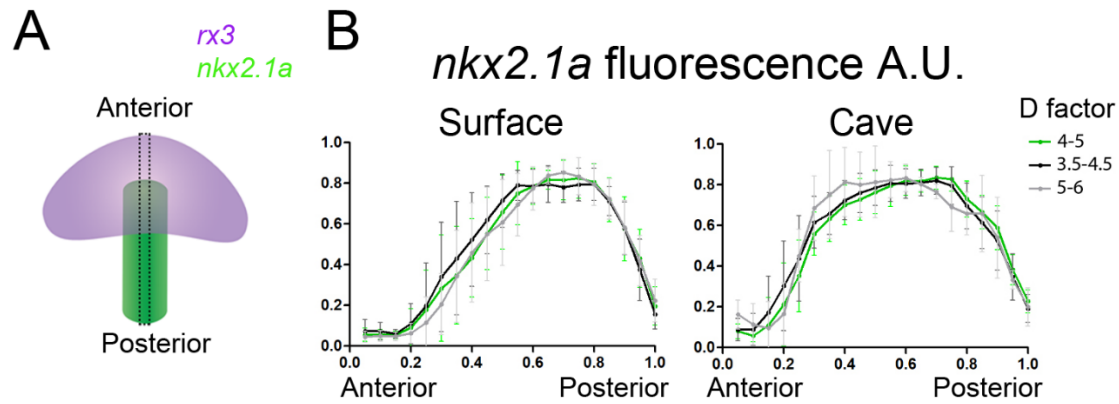
Fig. S7. Measurement of *nkx2.1a* fluorescence levels according to d factor. (A) Schematics of line A/P histogram quantification, line 50μm width from the anterior limit of *rx3* to the posterior limit of *nkx2.1a*. (B) *Nkx2.1a* fluorescence levels in surface (left) and cavefish (right) embryos according to different d factors. Two-ways ANOVA tests were performed.
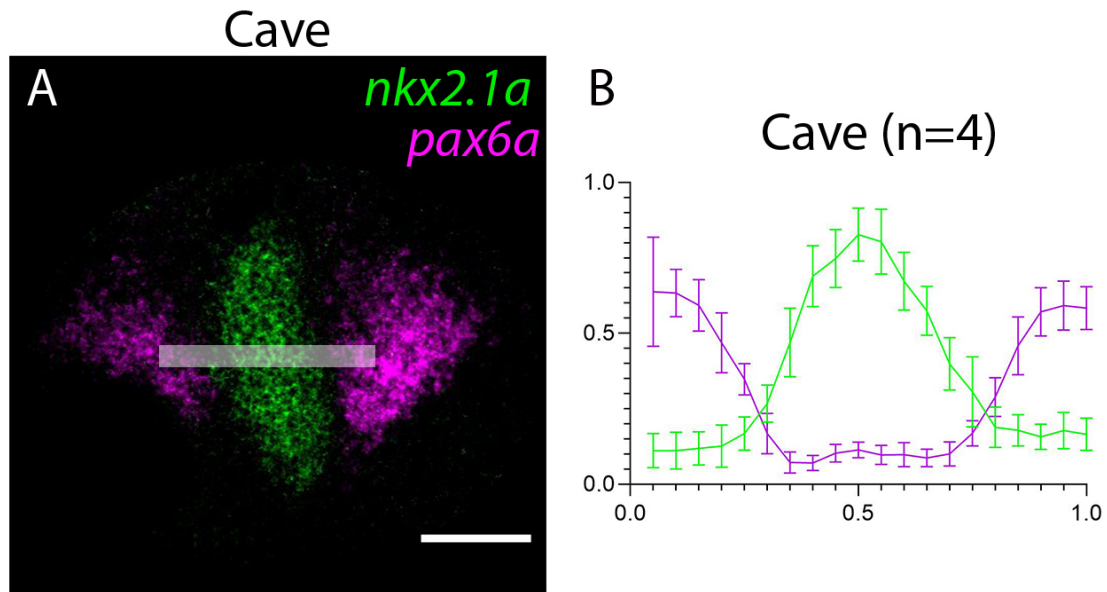
Fig. S8. Relative position of *pax6a* and *nkx2.1a* domains in the cave morph. (A) Maximum intensity projections of an intermediate substack (3 µm). (B) Plot profiles for *pax6a* and *nkx2.1a* (rectangle in A, 10 µm wide). As evidenced, a gap separates both domains in this morph, where *nkx2.1a* domain is expanded compared to surface fish. Scale bar 100 µm.
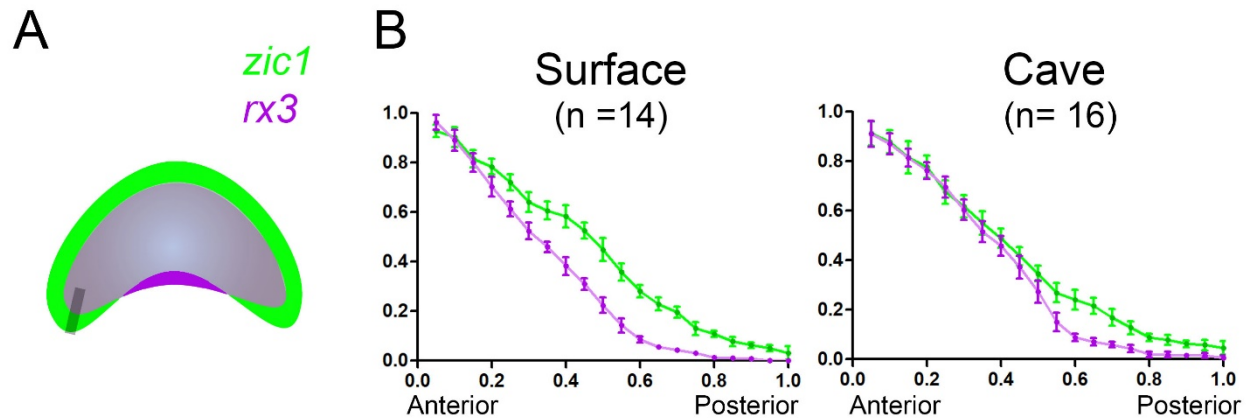
Fig. S9. Measurement of *zic1* and *rx3* fluorescence levels at the posterior limit of the eyefield. (A) Schematics of line A/P histogram quantification, line of 80µm width at the posterior limit of *zic1*. (B) *zic1* (green) and *rx3* (magenta) fluorescence levels in surface (left) and cavefish (right) embryos in the posterior limit of the eyefield (line in A).
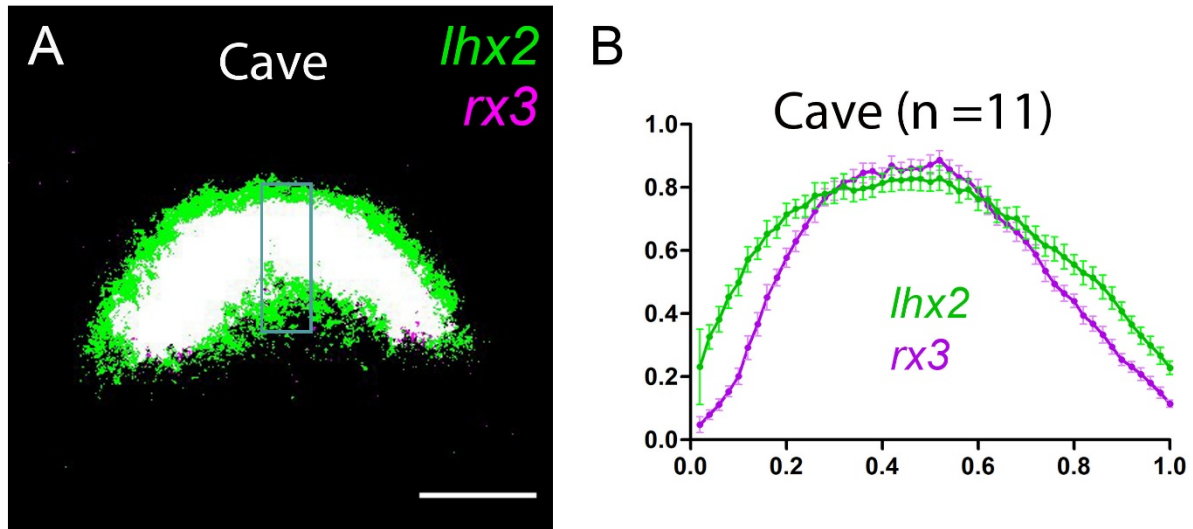
Fig. S10. Measurement of *lhx2* and *rx3* fluorescence levels at the ANP midline in cavefish. (A) Binary image of a full stack maximum intensity projection showing anterior position of lhx2 expression domain compared to *rx3* in cavefish. (B) Averaged plot profile according to ROI (A, rectangle) for the indicated number of cavefish samples.

.
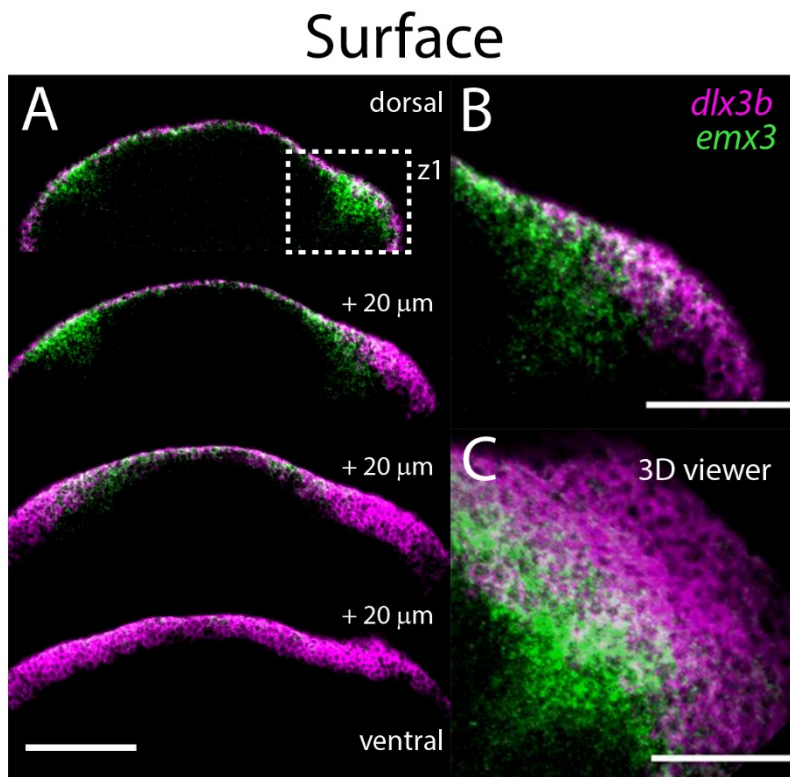
Fig. S11. Images of double fluorescent ISH showing *dlx3b* and *emx3* relative lateral posterior positions in the ANP. (A) Montage of 4 different maximum intensity projections (3 μm) in the DV axis. (B-C) Dorsal views of 3D renditions obtained by 3D stack projection (B) and 3D stack viewer (C) corresponding to square in A. Scale bar, 100 μm.
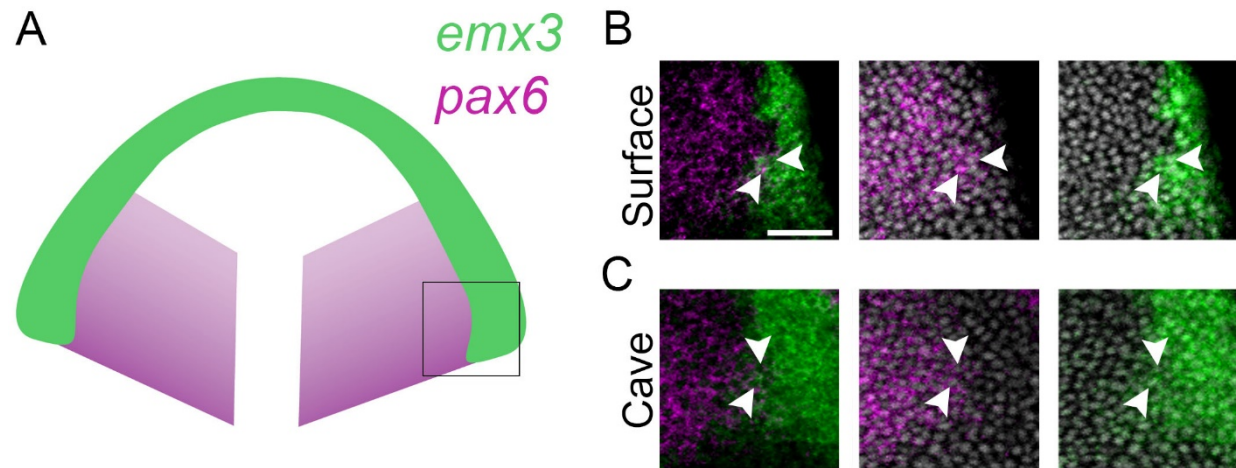
Fig. S12. Existence of a small *pax6a* and *emx3* lateral posterior domain in the ANP. (A) Schematics of the *emx3* and *pax6* expression domains. Black square indicates the region that is zoomed in B-C. (B-C) expression of *emx3* and *pax6* in the posterior ANP domain in surface fish (B) and cavefish (C). Arrowhead point to cells expressing both markers. Staining with DAPI was used to identify individual nuclei (greys). Scale bar, 50 μm.
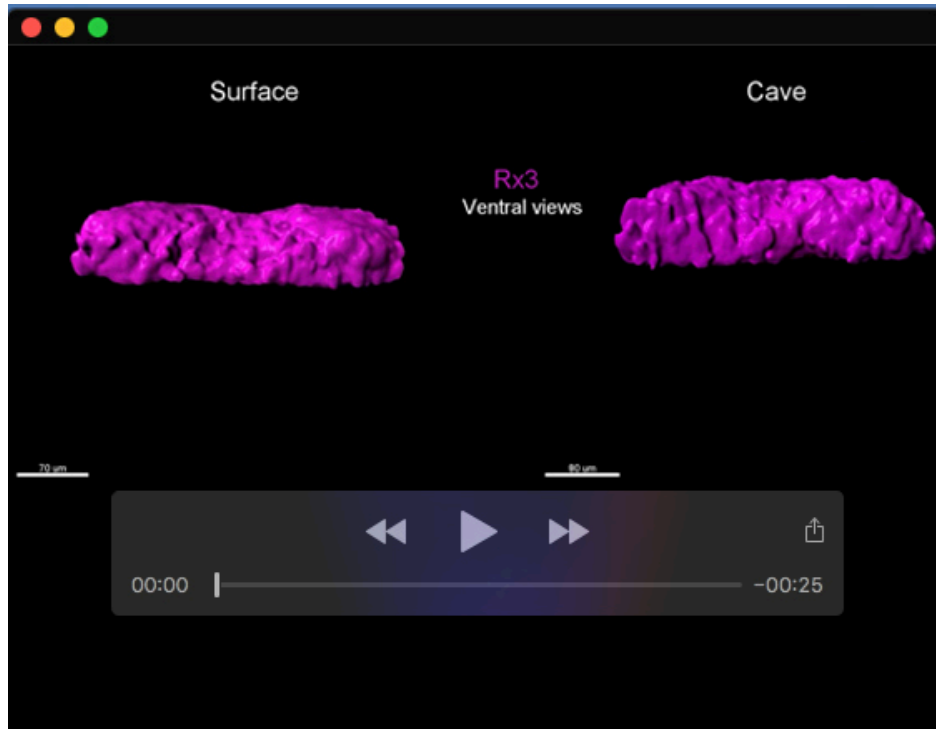
Movie 1. Comparison of *rx3* domain 3D shape in surface fish and cavefish.
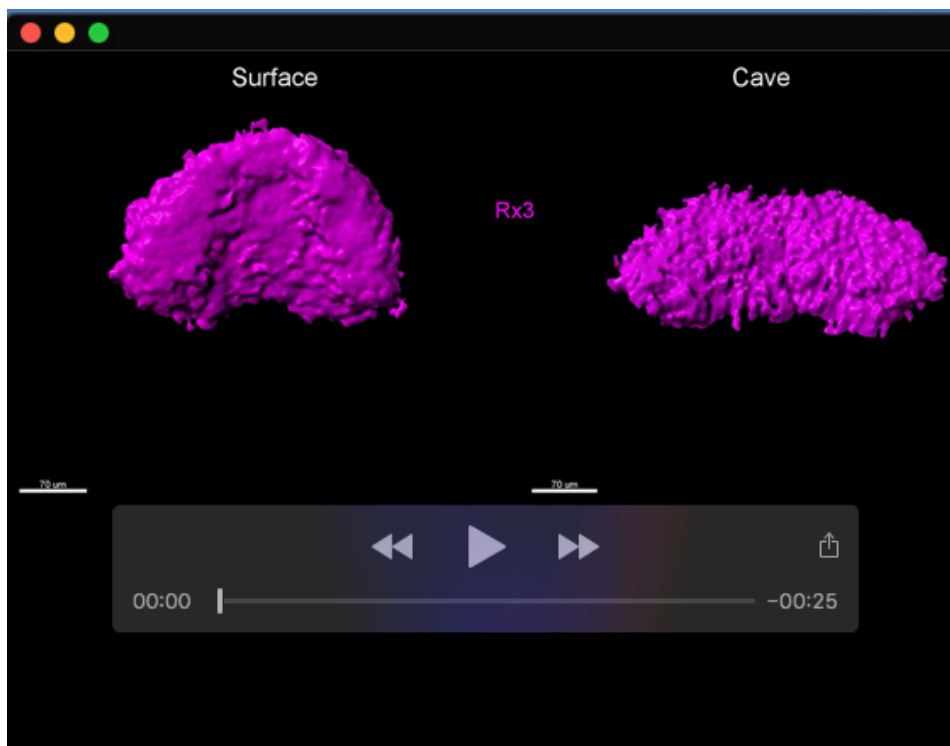
Movie 2. Highlighting *cxcr4b* subdomain in surface fish and cavefish.
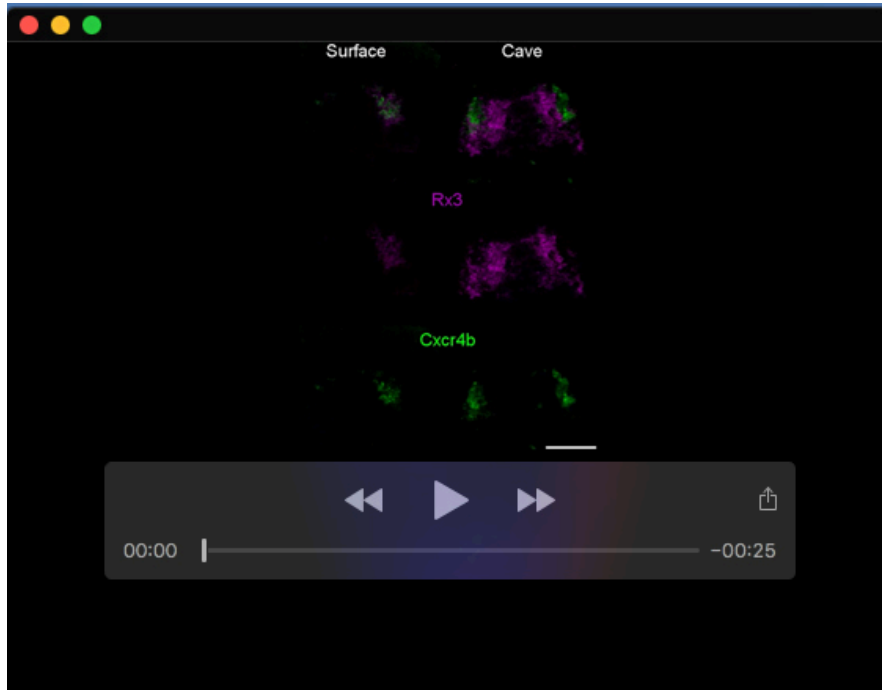
Movie 3. Highlighting *cxcr4b* and *rx3* complementary expression in cavefish ANP.
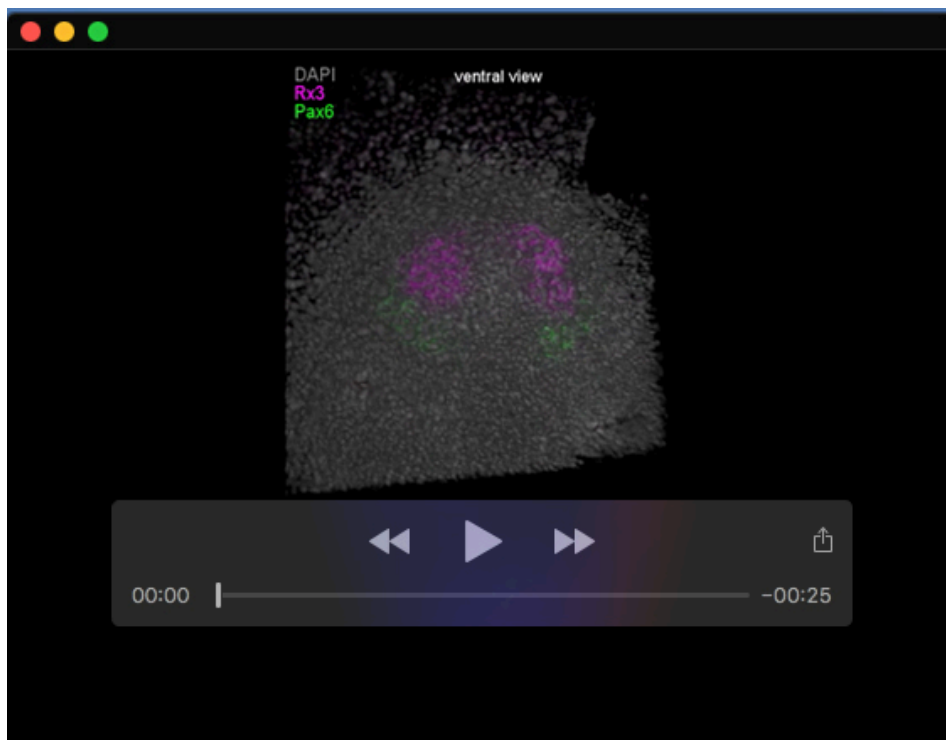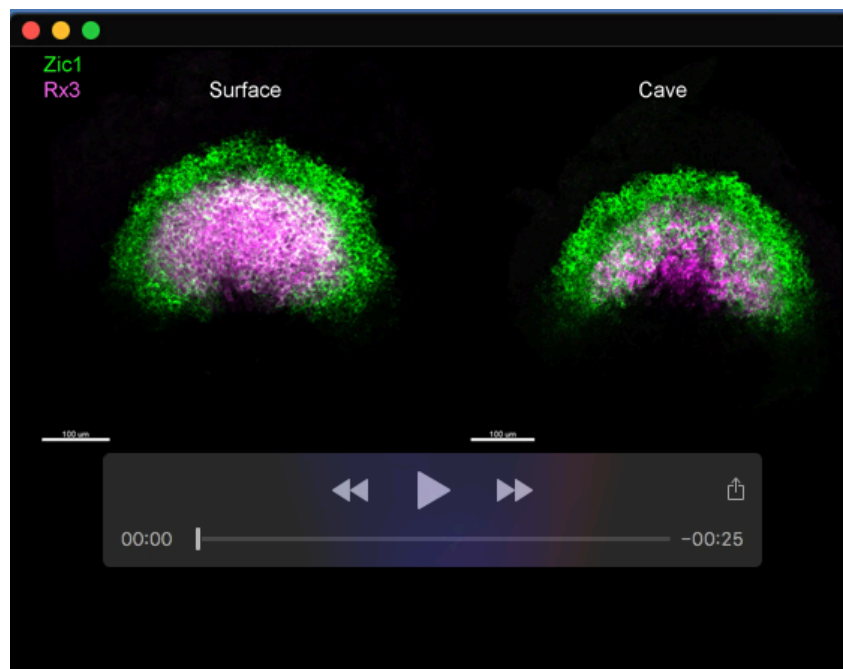

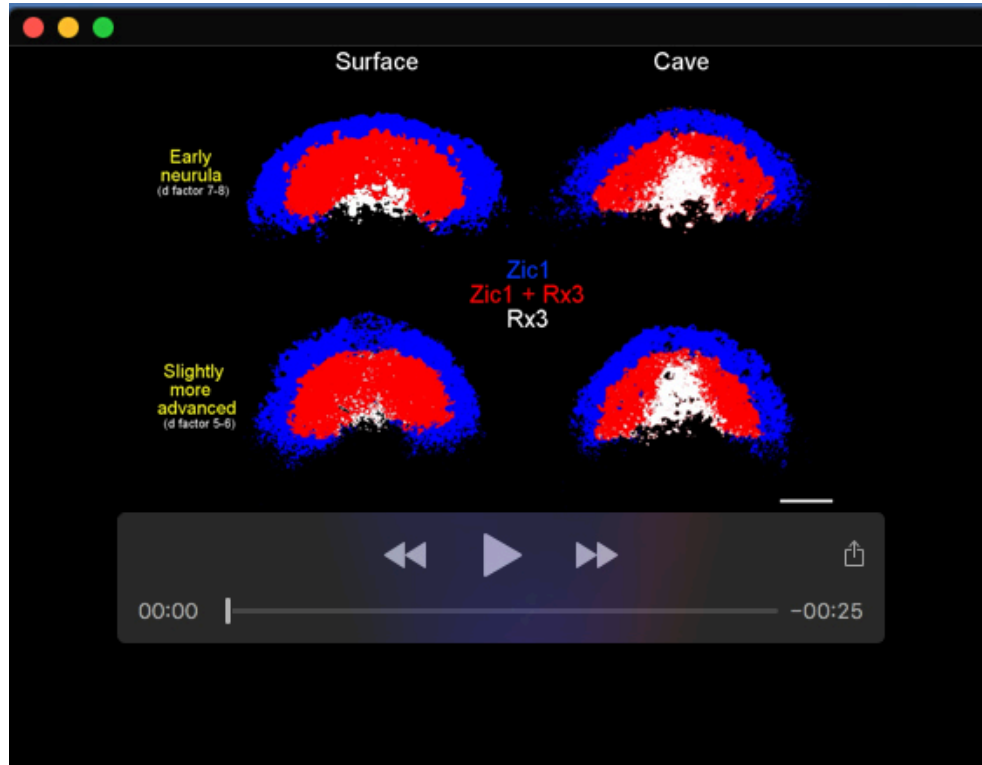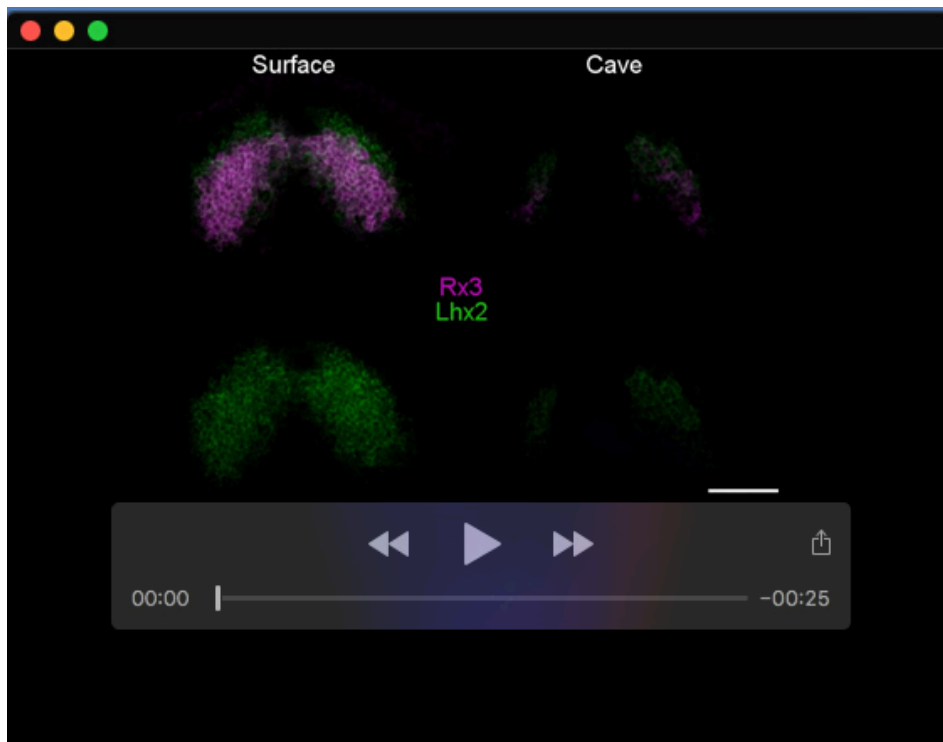**Movie 4.** Anteroposterior eyefield regionalization in 3D.
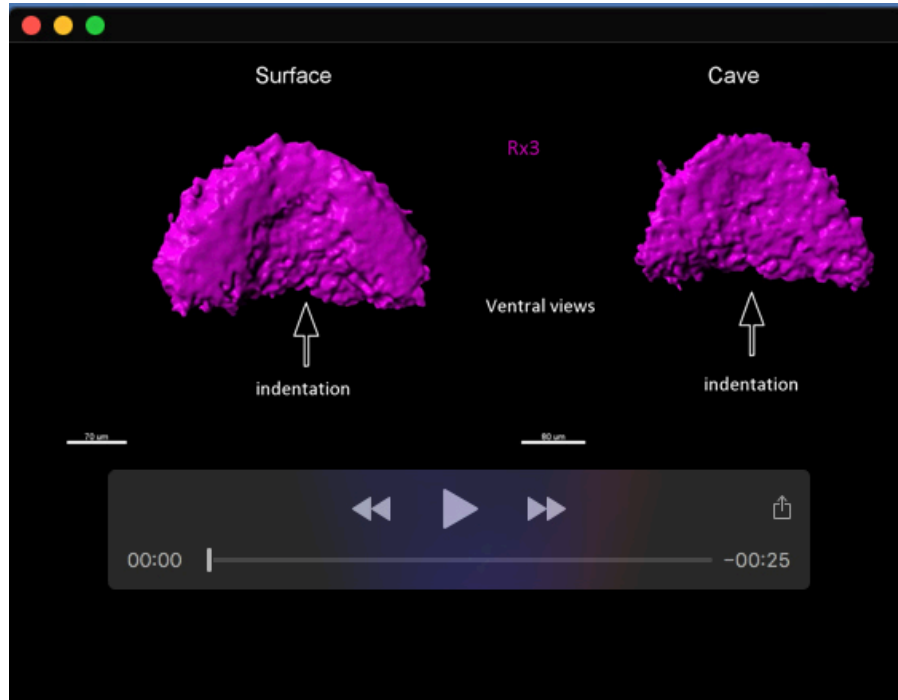
Movie 5. Relative position of the prospective hypothalamus and eyefield in 3D and domain interface size and shape.
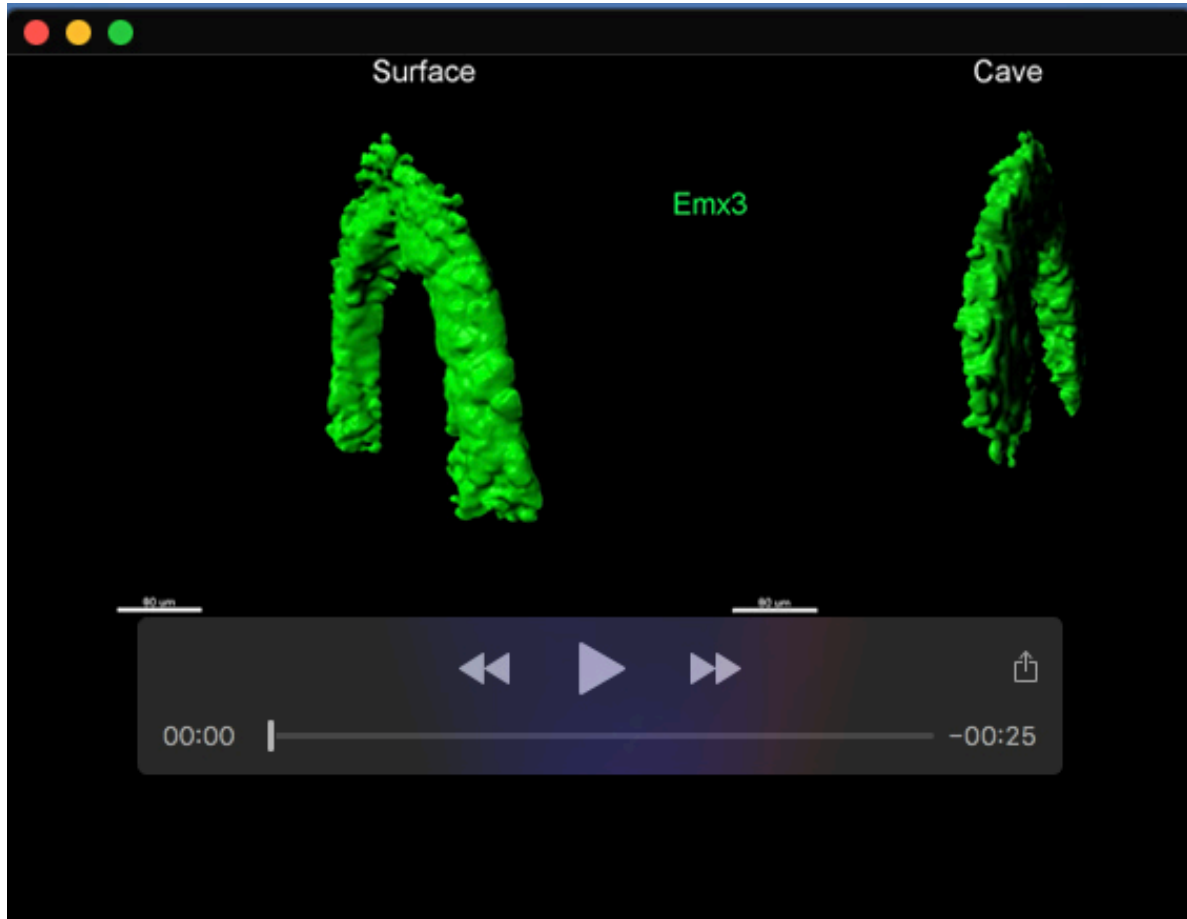

Movie 6. Major subdivisions in the anterior eyefield revealed by *zic1* and *rx3*.

Movie 7. Enlargement of the only *rx3*-expressing ventral midline eyefield subdivision in cavefish.

Movie 8. Highlighting slight anterior position of *lhx2* expression in surface fish and cavefish ANP.

Movie 9. 3D comparison of the eyefield and prospective telencephalon interface in surface fish and cavefish.